

# Review of the experimental and theoretical landscape of electron transport in noble liquids

G. J. Boyle<sup>1,\*</sup>, N. A. Garland<sup>2,3,\*</sup>, D. L. Muccignat<sup>1</sup>, I. Simonović<sup>4</sup>,  
D. Bošnjaković<sup>4</sup>, S. Dujko<sup>4</sup> and R. D. White<sup>1</sup>

<sup>1</sup>College of Science and Engineering, James Cook University, Townsville, Australia

<sup>2</sup>Queensland Quantum and Advanced Technologies Research Institute, Griffith University, Nathan, Australia

<sup>3</sup>School of Environment and Science, Griffith University, Nathan, Australia

<sup>4</sup>Institute of Physics, University of Belgrade, Belgrade, Serbia

Correspondence\*:

G. J. Boyle, N. A. Garland

gregory.boyle@jcu.edu.au, n.garland@griffith.edu.au

## ABSTRACT

We present a review of the current experimental and theoretical understanding of electron transport in noble liquids. Special attention is given to recent measurements that coincide with the development of time projection chambers (TPCs) using liquid xenon and argon as detector media. To enable transparent benchmarking of simulations and to facilitate the comparison between early studies and modern TPC data, we introduce a new open-access database of electron mobility and diffusion measurements. In particular, we emphasize the transition to large-scale detector designs which incorporate extended drift distances alongside improved purity control and field uniformity. On the theoretical side, we contrast empirical transport models with *ab initio* approaches, highlighting our recent efforts to incorporate low-energy, liquid-specific scattering phenomena, including coherent scattering, polarization screening, and bulk potential modifications. While elastic transport has seen substantial theoretical progress, inelastic processes in liquids, including ionization, exciton formation and interband transitions, remain poorly understood due to the lack of experimental cross sections

and validated models. We also discuss the applications and challenges of modeling scintillation, doped and mixture-liquid targets, and gas–liquid interface behavior, all of which are critical for the design and optimization of next-generation detectors.

**Keywords:** electron transport, noble liquids, swarm experiments, time projection chambers, liquid xenon, liquid argon

## 1 INTRODUCTION

The transport of free electrons in dense fluids, particularly in liquefied noble gases such as argon and xenon, plays a central role in both fundamental physics and detector technology. These systems lie at the intersection of condensed matter, atomic physics, and high-energy physics, and underpin some of the most sensitive experimental searches for rare processes, including neutrino interactions and dark matter detection.

Liquid-phase noble gas detectors, especially those employing time projection chamber (TPC) designs, have become indispensable in astroparticle and neutrino physics. Simultaneous measurements of scintillation light and ionization charge signals allows precise event reconstruction. Recent large-scale experiments, including XENONnT (Aprile et al., 2019), LZ (Aalbers et al., 2023),

PandaX (Liu, 2022), ProtoDUNE (Abi et al., 2020), MicroBooNE (Abratenko et al., 2021b), and ICARUS (The ICARUS Collaboration, 2004), demonstrate this approach's maturity, with tonne- to hundred-tonne-scale active masses now routine (Colaleo et al., 2021). For example, TPCs that use a LXe target have set world-leading limits on WIMP-nucleus cross-sections in the  $\text{GeV}/c^2$  to  $\text{TeV}/c^2$  mass range (Schumann, 2019).

In such detectors, particle interactions within the liquid target medium produce excited and ionized atoms. Scintillation photons offer a prompt time reference, while free electrons liberated by ionization are drifted under electric fields across the liquid-gas interface and are subsequently extracted. The fidelity of the signal reconstruction and hence the detector's sensitivity depends critically on our understanding of how electrons move through the liquid. Properties such as drift velocity, diffusion, and recombination all influence the shape and timing of the charge signal.

To probe these transport properties, dedicated electron swarm experiments have been employed since the mid-20th century, many using time-of-flight (TOF) techniques. In these studies, a short electron pulse is produced (typically from a photocathode) and tracked as it drifts and diffuses under the influence of an electric field. Some setups incorporate transverse magnetic fields to probe combined electric-magnetic field effects (Lamp and Buschhorn, 1994). Careful control of the thermodynamic state of the liquid, typically achieved by regulating temperature, pressure, and density, allows measurements over a broad range of physical conditions. Transport properties, such as mobility, characteristic energy, diffusion coefficients and the ionization rate, are then extracted from the evolution of the electron cloud. These properties feed directly into models for detector simulation and plasma behavior (Makabe and Petrovic, 2006; Petrović et al., 2009; Robson et al., 2017), or can be used to extract underlying electron-atom scattering cross-sections via inverse swarm analysis (Engelhardt and Phelps, 1963;

Engelhardt et al., 1964; Morgan, 1991; Stokes et al., 2020; Muccignat et al., 2024).

Despite the widespread availability of gas-phase transport data, consolidated in databases like LXCat (Pitchford et al., 2017; Carbone et al., 2021) and NIST (Lemmon, 2025), corresponding liquid-phase data remain fragmented and incomplete. In particular, few comprehensive datasets exist for liquids, especially in conditions relevant to modern TPCs. Furthermore, while simplified scaling laws often attempt to bridge gas and liquid regimes, this approach is generally insufficient due largely to the increased density effects that become important for electrons scattering in liquids compared to gases (see Section 3.2).

In 1965, Schnyders and collaborators questioned the applicability of gas-phase cross-sections in dense media (Schnyders et al., 1965). Their subsequent work proposed that a more accurate description could be achieved by including interference effects via the liquid structure factor (Schnyders et al., 1966). These insights, together with theoretical advancements by Cohen and Lekner (Lekner, 1967; Cohen and Lekner, 1967), laid the foundation for the modern understanding of electron transport in dense atomic fluids. The increased density introduces short-range order and coherent scattering effects, fundamentally altering the electron's potential landscape. Early theoretical treatments addressed these issues by modifying the effective interaction potential to account for the medium interparticle correlations (Lekner, 1967; Cohen and Lekner, 1967; Schmidt, 1984; Sakai et al., 1982, 1985; Sakai, 2007; Atrazhev and Iakubov, 1981; Atrazhev and Timoshkin, 1996, 1998). Atrazhev and collaborators further demonstrated that, at low energies, cross-sections become nearly energy-independent and scale primarily with density (Atrazhev and Iakubov, 1981; Atrazhev and Timoshkin, 1996, 1998). In a later refinement, Atrazhev et al. (1995) introduced a variable-phase-function method and muffin-tin potentials to incorporate liquid structure more realistically.

From an empirical perspective, Sakai and co-workers (Sakai et al., 1985; Sakai, 2007) used a fitting procedure to adjust the momentum transfer cross-sections to match swarm data. Borghesani and co-workers (Borghesani and Santini, 1994; Borghesani, 2006, 2014) developed a heuristic for constructing an effective momentum transfer cross-section from modified gas phase cross-sections, thereby accurately predicting enhancements (or reductions) in the zero-field mobility. Sophisticated treatments that use a Green's function method were employed by Braglia and Dallacasa (1982) to explore electron self-energy corrections, though such models are often limited by assumptions like linear response and near-equilibrium conditions.

Our recent work aims to develop a unified *ab initio* model for electron transport in noble liquids and dense gases, leveraging highly accurate electron-atom potentials benchmarked in the gas phase (Boyle et al., 2015, 2016; White et al., 2018). This framework avoids oversimplified potentials, e.g. the Buckingham potential, which neglect exchange interactions. The use of accurate potentials yields excellent agreement of transport coefficients calculated via a Boltzmann Equation (BE) solver with experimental data in the elastic scattering regime. However, extending this framework to incorporate inelastic processes, such as excitation and ionization, remains a frontier. Inelastic processes suppress coherence and introduce additional complexities, including threshold energy shifts and band structure formation (Reininger et al., 1983; Simonović et al., 2019). Emerging tools such as machine learning may offer a valuable method to interpolate and validate cross-section models against liquid-phase data, but such efforts will require tight coupling between theory and precision measurement.

Scintillation and luminescence underpin the operation of modern particle detectors, with signal formation driven by the creation of ion-electron pairs and the radiative decay of excimers formed in the liquid environment, and is thus intimately connected to ionization and excitation processes. Detector performance is highly sensitive to the

microscopic details of these interactions, as well as to macroscopic effects such as impurity levels and the use of dopants, which can significantly alter light yield, spectral response, and charge transport characteristics.

The macroscopic behavior of electron swarms in the detector medium is characterized by transport coefficients. A longstanding challenge in interpreting swarm data lies in the precise definition and measurement of these transport coefficients (Sakai et al., 1977; Tagashira et al., 1977; Robson, 1984, 1986; Kondo and Tagashira, 1990; Robson, 1991), and misunderstandings still persist. In the hydrodynamic regime, the space-time dependence of all macroscopic quantities can be projected onto the electron number density  $n(r, t)$  (Kumar et al., 1980), and distinctions must be made between flux coefficients (those appearing in flux-gradient relations like Fick's law) and bulk coefficients (those that describe the evolution of the entire cloud). These quantities can differ significantly in the presence of non-conservative processes such as ionization, attachment, or strong field gradients (Sakai et al., 1977; Tagashira et al., 1977; Robson, 1984). Although TPCs typically operate at low reduced electric field strengths in atomic liquids, there can be strong fields near the extraction region and the presence of impurities can selectively remove free electrons, and a formal kinetic or fluid model analysis is recommended.

In this work, we compile and critically examine the body of available measurements of electron transport in liquid xenon (LXe) and liquid argon (LAr). By making this dataset more accessible, we hope to support the broader community engaged in simulation, modeling, and detector design. Beyond the experimental survey, we also review the theoretical frameworks that have been developed to describe electron transport in atomic liquids. Special attention is given to recent advances, including *ab initio* and semi-empirical models. New simulation tools, including emerging machine learning methods, offer new opportunities to inform detector development, particularly in regimes where direct measurements are difficult or incomplete.

In Section 2, we review the current status of swarm experiments that measure electron mobility and diffusion in LAr and LXe, with a focus on results driven by TPC applications. Section 3 examines the theoretical and simulation landscape, outlining how electron transport in noble liquids can be modeled from first principles and emphasizing key density effects, including elastic coherent scattering, bulk potential modifications, and the formation of excitation band-structures. In Section 4, we focus on selected topical applications and experimental challenges in liquid detector development, covering topics such as scintillation modeling, the behavior of doped and mixed-liquid systems, and electron transport across gas-liquid interfaces. We conclude with a summary of current challenges and a forward-looking perspective on how modern modeling approaches and data-driven tools can shape the future of electron transport studies in noble liquid detectors.

## 2 NOBLE LIQUID SWARM EXPERIMENTS

This section surveys key experimental efforts, as introduced in Section 1, to measure electron transport properties, specifically mobility and diffusion coefficients, in LAr and LXe. These measurements serve as essential benchmarks for validating the theoretical frameworks discussed in Section 3.

Early experiments generated electron swarms using radioactive sources placed near the cathode (Williams, 1957). Ionizing radiation from these sources produced electron–ion pairs *in situ*, which were then accelerated through the liquid and collected at the anode (Davidson and Larsh, 1950; Eibl et al., 1990). While effective, these methods offered limited control over the initial distribution of electron energies and positions. Later techniques introduced more precise electron sources, such as photocathodes illuminated by pulsed lasers (Njoya et al., 2020) or discharge lamps (Eibl et al., 1990), allowing for better-defined injection profiles. Additional methods include field

emission from sharp metal electrodes immersed in the liquid (Halpern et al., 1967) and electron beams fired directly into the target medium (Miller et al., 1968).

While the basic operating principles remain similar, modern large-scale detectors differ significantly from earlier laboratory-scale experiments. In particular, drift lengths have increased from millimeter–centimeter scales to distances of up to several meters (Colaleo et al., 2021). This scaling introduces new challenges in maintaining field uniformity, ensuring liquid purity, and understanding long-range effects on charge transport.

Despite their utility, TOF experiments are subject to several sources of systematic uncertainty. One of the most important is the purity of the liquid. In the foundational experiments, impurities such as oxygen may have gone uncharacterized, potentially introducing electron attachment processes that distort transport measurements (Baudis et al., 2023). In contrast, modern detectors benefit from advanced purification systems and use attachment rate measurements as a diagnostic for liquid purity.

Another challenge lies in accurately modeling the initial electron distribution. Techniques based on ionizing radiation tend to produce poorly defined spatial and energy profiles, which complicates direct comparison with simulations. Laser-based photoemission sources offer greater control but require precise alignment and timing. Similarly, improvements in cryogenic engineering now allow more accurate control of temperature, pressure, and density—properties that are essential for modeling the system's phase and state variables. Earlier studies may lack this level of detail and, in such cases, approximations must be made to reconstruct the operating conditions and enable comparison with theory.

Additionally, assumptions of uniform electric fields may not hold near electrodes, where field distortions can affect drift and diffusion. This can introduce bias when interpreting TOF data, particularly for short drift lengths or near-surface effects. Since the TOF method averages transport

properties over the full drift region, it is inherently limited in its ability to resolve spatial variations or localized inhomogeneities in the liquid.

Nonetheless, TOF remains one of the most powerful and widely used techniques for probing electron transport in atomic liquids. When conducted under well-characterized conditions, these experiments provide critical data for developing and validating theoretical models, as well as informing the design and operation of noble-liquid-based detectors.

## 2.1 Select measurements of electrons in LXe and LAr

As noted in Section 1, tabulated transport coefficients and scattering cross-sections play a vital role in plasma modeling and in enabling transparent, quantitative comparisons across different experimental studies. Over the past decade, the expansion of experimental datasets has also enabled data-driven approaches, most notably deep learning techniques, to infer electron scattering cross-sections from measured transport properties (Stokes et al., 2020; Jetly and Chaudhury, 2021; Muccignat et al., 2024). To date, most databases (including LXCat and NIST) have focused primarily on electron transport in the gas phase. However, recent developments have begun to broaden this scope. For example, LXCat has announced an updated version of its database that will incorporate new states of matter and broader classes of incident particles (Boer et al., 2023).

In this section, we present representative data on the electron mobility and diffusion coefficients in LXe and LAr over a range of experimental conditions. The full dataset is available on GitHub<sup>1</sup> and is structured in a format similar to LXCat. While CSV formats were initially used, we are exploring alternative text-based formats to better support transparency and long-term maintainability. A complete list of the data in the repository is available in Appendix 1.

These representative samples highlight both the range of experimental behavior observed and the degree of consistency between early pre-2000 measurements and more recent studies motivated by large-scale liquid TPC development. Because published transport data are typically reported as functions of the absolute electric field at fixed temperatures and pressures, we have converted the data into reduced quantities (e.g.,  $E/N$ ) using reported liquid densities where available. In cases where the density is not given, we estimate it along the saturated liquid line using interpolated data from the NIST Chemistry WebBook<sup>2</sup> database of Thermophysical Properties of Fluid Systems (Lemmon, 2025).

Transport in these systems is often modeled using the drift-diffusion equation (Huxley and Crompton, 1974), which requires knowledge of drift velocity (mobility), swarm broadening (diffusion), and net particle production or loss (ionization or attachment). In noble liquids, at low fields, electron impact ionization does not occur and attachment is negligible in pure media. However, even trace impurities such as oxygen or water vapor can introduce attachment pathways, emphasizing the importance of high-purity conditions in experiments. For TPC applications, high mobility and low diffusion are especially desirable, motivating the use of liquid-phase detectors.

The top panel of Figure 1 shows the reduced electron mobility in LXe as a function of reduced electric field, spanning more than 50 years of measurements. The data are grouped by background temperature and compared to empirical fits from the NEST simulation framework (Szydagis et al., 2022, 2025).

Recent measurements have largely been limited to low reduced fields ( $E/N < 0.01$  Td), making high-field behavior less well characterized. The TPC data suggest higher mobilities at similar conditions, e.g., when comparing the data of Huang and

<sup>1</sup> Liquid Transport Data - [www.github.com/jcu-transport-physics/liquid-transport-data](https://www.github.com/jcu-transport-physics/liquid-transport-data)

<sup>2</sup> NIST Standard Reference Database 69: NIST Chemistry WebBook - <https://doi.org/10.18434/T4D303>

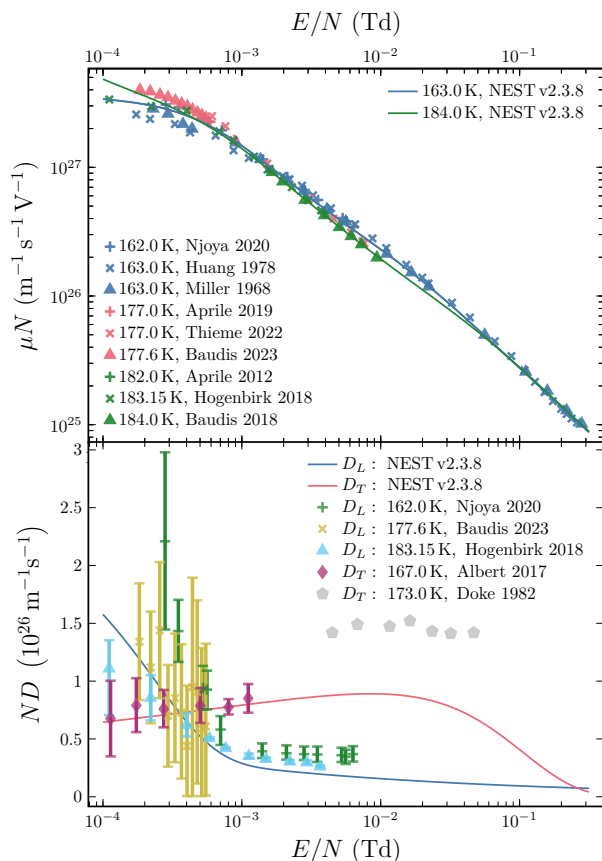


**Figure 1.** Top: Experimental reduced mobility ( $\mu N$ ) as a function of reduced electric field ( $E/N$ ) for LXe restricted to three groups of temperatures. Each color represents a different temperature grouping. Solid lines are the empirical curves from NEST (Szydakis et al., 2022). Bottom: Experimental reduced diffusion coefficients ( $ND_L$  and  $ND_T$ ) as a function of reduced electric field from select authors for LXe. Solid lines are the empirical curves from NEST.

Freeman (1978); Miller et al. (1968), and that of Njoya et al. (2020). This may reflect differences in experimental design, particularly liquid purity and field uniformity. The mobility curves at 177 K and 183 K exhibit slightly different slopes compared to those at 163 K, potentially pointing to temperature-dependent structural changes or impurity effects. The NEST simulation results align well with all measurements, favoring the more recent measurements at low fields, although this agreement likely reflects the empirical basis of the model. As Baudis et al. (2023) notes, impurities such as water vapor and hydrocarbons can serve as

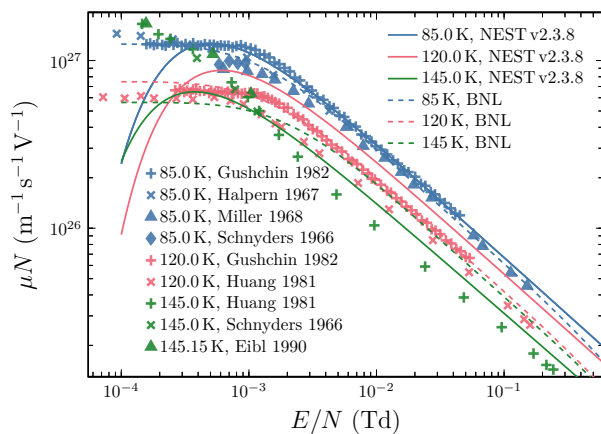
additional energy-loss channels, leading to higher mobility and suppressed diffusion. This may help explain the elevated drift velocities reported in early studies such as Gushchin et al. (1982), where purification methods were not documented.

Figure 1 also presents reduced longitudinal and transverse diffusion coefficients in LXe, in the bottom panel. Although uncertainties are significant, the longitudinal diffusion coefficients decrease with increasing field strength, while the transverse diffusion coefficients appear largely field-independent within each dataset. The trends in the longitudinal diffusion are broadly consistent with NEST simulations, though further high-precision measurements would help constrain the full field dependence and reduce uncertainty. The NEST curve for the transverse diffusion coefficient has been determined from the experimental measurements of Albert et al. (2017), but underestimates the measurements at higher fields from Doke (1982) (which has an estimated uncertainty of approximately  $\pm 10\%$  (Doke, 1981)). Clearly, a single model consistent with the full range of LXe transport coefficients is still elusive.

Figure 2 shows the reduced mobility of electrons in LAr, with data grouped by temperature over the range of 85 K to 150 K. The results show considerable variation in both plateau values and field dependence, reflecting the underlying temperature sensitivity of the medium's structure. In particular, the nonlinear temperature dependence of the pair correlation function and the static structure factor plays a key role at low fields.

Within each temperature group, measurements are generally consistent, with the exception of the early results reported by Gushchin et al. (1982), which again appear anomalously high when compared to recent experiments. These discrepancies are likely attributable to uncharacterized impurities.

Temperature clearly plays an important role in determining transport behavior, not just through thermal velocity distributions, but also via structural correlations in the liquid. This sensitivity presents challenges for empirical modeling. The NEST



**Figure 2.** Experimental reduced mobility ( $\mu N$ ) as a function of reduced electric field  $E/N$  for LAr, restricted to three groups of temperatures. Each color represents a different temperature grouping. Solid lines are the empirical curves from NEST (Szydakis et al., 2022). Dashed lines are the empirical curves from BNL (Li et al., 2016)

profiles do a sensible job of representing the mobility data at reduced fields above 0.001 Td, but break down at low fields. The Brookhaven National Laboratory (BNL) tool's empirical fit (Li et al., 2016) performs reasonably well at 85 K and 120 K but fails to reproduce data at 145 K. This highlights a broader problem: empirical models often lack predictive power outside the narrow conditions for which they were calibrated, reinforcing the need for *ab initio* approaches that incorporate medium structure and density effects explicitly.

Although LAr and LXe are the most studied noble liquids, other systems have also been investigated. Measurements in liquid krypton are broadly consistent with LAr and LXe results (Nishikawa et al., 2007; Schnyders et al., 1966), showing intermediate behavior. In contrast, transport in neon and helium shows marked differences due to their unique electronic properties. Neon and helium have low polarizability and exhibit positive scattering lengths due to Pauli exclusion, resulting in fundamentally different scattering dynamics (Bruschi et al., 1972; Sakai et al., 1982; Borghesani et al., 1988; Hernandez, 1991; Schmidt et al., 2003; Borghesani, 2021). These liquids support the formation of electron bubbles, i.e.,

quasi-stable low-density cavities, due to strong short-range repulsive forces (Hernandez, 1991). As a result, mobility in neon and helium is often lower in the liquid than in the gas phase. By contrast, in argon and xenon, attractive interactions promote electron localization at atomic sites, preventing bubble formation and leading to higher liquid-phase mobility (Borghesani et al., 1992; Borghesani, 2006). Electron localization and self-trapping is discussed further in Section 3.3.

### 3 THEORY AND SIMULATION

The transport of charged particles through gases and liquids is most rigorously described by Boltzmann's kinetic equation (BE). Since its introduction in the 19th century (Boltzmann, 1872), the BE has remained the gold standard for understanding the statistical behavior of charged particles in a wide range of systems (Cohen and Thirring, 1973; Boyle et al., 2023).

However, the BE approach is most effective in idealized scenarios i.e., those with simplified geometries, uniform media, and well-behaved boundary conditions. Real-world systems, particularly those relevant to detector physics, often involve complexities such as sharp interfaces, spatially varying fields, and secondary particle production. These features can make solutions of the deterministic BE intractable.

To address these challenges, stochastic methods, most notably Monte Carlo (MC) simulations (Skullerud, 1968; Park et al., 2023; Beever et al., 2024), have been widely adopted. Modern MC techniques, along with particle-in-cell or hybrid schemes, provide a powerful and flexible alternative to deterministic modeling (Tskhakaya et al., 2007). With the increasing availability of computational resources, these methods have become the preferred tool for exploring systems with complex spatial structures, non-linear effects, and multiple interacting particles. Previous studies have demonstrated the utility of MC simulations for modeling electron transport in both gas and liquid media (Emfietzoglou et al., 2003; Champion et al.,

2012; Petrović et al., 2014; Tattersall et al., 2015; Emfietzoglou et al., 2017; Mehnaz et al., 2020; Beever et al., 2024).

In the context of particle detectors, one of the most widely used MC-based tools is the Noble Element Simulation Technique (NEST) software (Szydagi et al., 2011, 2021, 2025). NEST has been extensively validated against experimental data and is frequently employed to simulate detector responses across a wide range of energies and electric field strengths. Its phenomenological approach enables practical modeling of scintillation and ionization signals in both gaseous and liquid systems. However, as noted in Szydagi et al. (2025), NEST relies heavily on empirical parameterizations which may introduce significant uncertainties when extrapolating to new energy regimes or electric field conditions where data is sparse or unavailable. Integrating *ab initio* scattering cross-sections and transport models into frameworks like NEST would represent an important step forward, reducing reliance on empirical tuning and enhancing predictive power.

While this section primarily focuses on the application of the BE to noble gas and liquid systems, many of the underlying scattering processes discussed, such as interference effects and potential modifications, are equally relevant to MC simulations. In practice, the most robust modeling strategies will combine the strengths of both deterministic and stochastic methods. Together, these approaches provide a complementary toolkit for the accurate simulation of electron transport in complex detector environments.

### 3.1 Multi-term solution of the Boltzmann kinetic equation

The behavior of electrons in gases and liquids under the influence of an external electric field  $\mathbf{E}$  is governed by the BE, which describes the evolution of the phase-space distribution function  $f(\mathbf{r}, \mathbf{v}, t)$ . This function represents the probability density for finding an electron with velocity  $\mathbf{v}$  at position  $\mathbf{r}$  and time  $t$ . The BE is (Boltzmann, 1872; Robson et al.,

2017):

$$\left( \frac{\partial}{\partial t} + \mathbf{v} \cdot \nabla + \frac{e\mathbf{E}}{m_e} \cdot \frac{\partial}{\partial \mathbf{v}} \right) f(\mathbf{r}, \mathbf{v}, t) = -J(f), \quad (1)$$

where  $e$  and  $m_e$  are the electron charge and mass, and  $J(f)$  is the collision operator describing interactions between electrons and the background medium.

In the dilute (or swarm) limit, where the electron population is sparse and does not perturb the background gas, the collision operator remains linear and can be decomposed into contributions from various interaction processes:

$$J(f) = J_{el}(f) + J_{ex}(f) + J_{at}(f) + J_{io}(f) + \dots \quad (2)$$

with  $J_{el}(f)$ ,  $J_{ex}(f)$ ,  $J_{at}(f)$ , and  $J_{io}(f)$  representing elastic scattering, excitation, attachment, and ionization, respectively. Boltzmann's original formulation only included elastic processes (Boltzmann, 1872), but subsequent extensions have incorporated inelastic collisions, particle creation and loss, quantum effects, and even relativistic or condensed-phase considerations (see Robson et al. (2017) for a review).

For systems involving electrons it is common to simplify the collision operator using a mass-ratio expansion in  $m_e/(m_e + m_0)$ , where  $m_0$  is the mass of the neutral target (Kumar, 1967; Robson et al., 2017). For light projectiles, only the first-order term is typically required, which simplifies the analysis significantly (Chapman and Cowling, 1970; Frost and Phelps, 1962; Kumar et al., 1980).

Number-conserving processes, such as elastic collisions and electronic excitations, are described using the semi-classical Wang Chang–Uhlenbeck–de Boer operator (Wang Chang et al., 1964). For excitation processes, this is expressed as:

$$J_{ex}(f) = \sum_{j,k} \int d\hat{\mathbf{g}} d\hat{\mathbf{v}}_0 g \sigma(j, k; g, \chi) \times [f(\mathbf{r}, \mathbf{v}, t) F_{0j}(\mathbf{v}_0) - f(\mathbf{r}, \mathbf{v}', t) F_{0j}(\mathbf{v}'_0)] \quad (3)$$

where  $j$  and  $k$  label the internal states of the background atoms,  $\sigma(j, k; g, \chi)$  is the differential cross-section for the transition  $(j, \mathbf{v}, \mathbf{v}_0) \rightarrow (k, \mathbf{v}', \mathbf{v}'_0)$ , and  $F_{0j}(\mathbf{v}_0)$  is the Maxwellian distribution for background atoms in state  $j$ . Energy conservation links the pre- and post-collision velocities via  $\frac{1}{2}m_e g^2 + U_j = \frac{1}{2}m_e g'^2 + U_k$ , where  $U_j$  and  $U_k$  are the internal energies of the respective states. When  $j = k$ , the collision represents an elastic scattering event. Modifications of the elastic scattering process in a dense gas or liquid medium, such as coherent scattering, are discussed in Section 3.2.

In contrast, non-conserving processes like electron attachment and ionization remove or create electrons, respectively. Attachment processes are described by:

$$J_{at}(f) = \sum_j f(\mathbf{r}, \mathbf{v}, t) \int d\mathbf{v}_0 g \sigma_{at}(j; g) F_{0j}(\mathbf{v}_0), \quad (4)$$

where  $\sigma_{at}(j; g)$  is the attachment cross-section for the  $j$ th attachment process. Ionization is represented as:

$$J_{io}(f) = \sum_j n_{0j} v \sigma_{io}(j; v) f(\mathbf{r}, \mathbf{v}, t) - 2n_{0j} \int d\mathbf{v}' v' \sigma_{io}(j; v') B(\mathbf{v}, \mathbf{v}'; j') f(\mathbf{r}, \mathbf{v}', t), \quad (5)$$

where  $\sigma_{io}(j; v)$  is the ionization cross-section for the  $j$ th process, and  $B(\mathbf{v}, \mathbf{v}'; j')$  is the probability distribution for the velocities of the outgoing electrons. Although ionization is fundamentally a three-body process, it is typically assumed that the heavy neutral remains stationary (valid to zeroth order in the mass ratio) so that energy and momentum are shared only between the incident and ejected electrons.

To solve the BE, a common strategy is to expand the distribution function in spherical harmonics,  $Y_m^{[l]}$  (Ness and Robson, 1986; Robson and Ness,

1986; Robson et al., 2017):

$$f(\mathbf{r}, \mathbf{v}, t) = \sum_{l=0}^{l_{\max}} \sum_{m=-l}^l f_m^{(l)}(\mathbf{r}, v, t) Y_m^{[l]}(\hat{\mathbf{c}}). \quad (6)$$

In systems with a preferred direction, such as those with a uniform electric field, this simplifies to a Legendre polynomial  $P_l$  expansion:

$$f(\mathbf{r}, \mathbf{v}, t) = \sum_{l=0}^{l_{\max}} f_l(\mathbf{r}, v, t) P_l(\cos \theta), \quad (7)$$

with  $\theta$  being the angle between the velocity vector and the electric field. Although the two-term approximation ( $l_{\max} = 1$ ) has been widely used for electrons, its limitations are well established (Robson and Ness, 1986; White et al., 2003; Petrović et al., 2009), and convergence must be tested by systematically increasing  $l_{\max}$ .

Various representations of the speed-space dependence of the coefficients in Equations (6)–(7) have been previously employed, including Sonine polynomials (Burnett, 1935, 1936), cubic splines (Pitchford et al., 1981; Penetrante et al., 1985), finite volume (Boyle et al., 2017), and finite difference schemes Maeda and Makabe (1994); Loffhagen and Winkler (1996); Sigeneger and Winkler (1996); Trunec et al. (2006); Stephens (2018). The combination of spherical harmonics and Sonine polynomials yields the well-known Burnett functions (Kumar, 1966; Burnett, 1935, 1936), which have played a critical role in the development of a unified solution to Boltzmann's equation across all mass ratios.

Regardless of the exact speed-space representation, substituting the angular expansion into the BE yields a hierarchy of coupled differential equations for the expansion coefficients  $f_m^{(l)}(\mathbf{r}, v, t)$ . In the spatially homogeneous steady-state case, these take

the form:

$$J^l(f_m^{(l)}) - \frac{eE}{m_e} \left( \frac{l+1}{2l+3} \left[ \frac{d}{dv} + \frac{l+2}{v} \right] f_m^{(l+1)} - \frac{l}{2l-1} \left[ \frac{d}{dv} - \frac{l-1}{v} \right] f_m^{(l-1)} \right) = 0, \quad (8)$$

where  $J^l$  denotes the spherical harmonic component of the collision operator.

Once these coefficients are known, key physical observables can be calculated. The electron number density  $n$  is given by:

$$n = 4\pi \int_0^\infty dv v^2 f_0^{(0)}(v), \quad (9)$$

and is typically normalized to unity. The flux drift velocity  $W$  is obtained from:

$$W = \frac{4\pi}{3} \int_0^\infty dv v^3 f_0^{(1)}(v), \quad (10)$$

while the mean energy  $\epsilon$  is:

$$\epsilon = 4\pi \int_0^\infty dv \frac{1}{2} m_e v^4 f_0^{(0)}(v). \quad (11)$$

Finally, the effective ionization coefficient (normalized to the neutral density  $N$ ) is expressed as:

$$\frac{R}{N} = 4\pi \int_0^\infty dv v^3 [\sigma_{gain}(v) - \sigma_{loss}(v)] f_0^{(0)}(v), \quad (12)$$

where  $\sigma_{gain}$  and  $\sigma_{loss}$  include all relevant cross-sections for particle-creating and particle-depleting processes, respectively.

To extend these results beyond spatial homogeneity, the distribution functions  $f_m^{(l)}(\mathbf{r}, v, t)$  can be expanded in terms of spatial and temporal gradients. This formalism connects directly to hydrodynamic transport coefficients, including bulk and flux mobilities and diffusion tensors, thus providing a bridge between microscopic kinetics and macroscopic fluid descriptions (Robson et al.,

2017; Robson and Ness, 1986; Ness and Robson, 1986; White et al., 2009).

There are often multiple common ways of presenting the same physical phenomena, which can depend on the exact type of measurement undertaken. For instance, the electron mobility  $\mu = W/E$  (or reduced electron mobility  $N\mu$ ) is often tabulated instead of the drift velocity, while the ionization coefficient  $\alpha \approx R/W$  is measured in a steady-state Townsend experiment Huxley and Crompton (1974); Dujko et al. (2008). The transverse diffusion coefficient  $D_T$  is routinely combined with the mobility  $\mu$  and presented as the characteristic energy,  $\frac{3}{2}D_T/\mu$ .

## 3.2 Electron swarms in atomic liquids

### 3.2.1 Interference effects

In dense media such as liquid noble gases, the transport of electrons differs significantly from that in dilute gases due to the emergence of quantum interference effects. These effects arise when the de Broglie wavelength of an electron becomes comparable to the average spacing between atoms in the medium. Under such conditions, scattering can no longer be treated as isolated binary collisions. Instead, electrons scatter coherently from multiple, spatially and temporally correlated atoms, leading to interference phenomena that are absent in low-density environments.

At intermediate densities, where the electron's mean free path remains much larger than its de Broglie wavelength, coherent scattering can be modeled under the single-scatterer approximation. In this regime, the medium is treated as a single extended scattering center with spatial correlations encoded through the structure of the surrounding atoms (Cohen and Lekner, 1967). This coherent elastic scattering effectively modifies the angular dependence of the collision process but does not apply to inelastic interactions. Processes such as excitation and ionization involve localized energy transfer and thus disrupt the phase coherence required for interference. As a result, interference effects are considered only in elastic channels.

As density increases further, the electron's mean free path can approach its thermal de Broglie wavelength. As described in the review by Borghesani (2006), in this regime the electron wavefunction may interfere with itself along time-reversed paths that scatter off neighboring atoms. This quantum self-interference leads to enhanced elastic backscattering and contributes to the suppression of electron mobility. At very high densities, these effects can become strong enough to induce a mobility edge (Polischuk, 1984), signifying a transition to localized transport reminiscent of Anderson localization in disordered solids. Such behavior marks the onset of a qualitatively different transport regime, where interference effects dominate over collisional scattering.

In typical noble-liquid detector environments, the atomic number density is  $1 - 2 \times 10^{28} \text{ m}^{-3}$ , corresponding to Wigner–Seitz cell radii of approximately  $5a_0$ . The de Broglie wavelength of electrons with energies below 10 eV is greater than  $7a_0$ , necessitating the inclusion of interference effects.

To incorporate these effects quantitatively, the elastic collision operator in the BE is modified through structure-dependent corrections. The Legendre components of the collision operator accounting for coherent scattering are given by:

$$J_0(\Phi_0) = \frac{m_e}{m_0 v^2} \left[ v \nu_1(v) \left( v f_l + \frac{k_b T}{m_e} \frac{d}{dv} f_0 \right) \right], \quad (13)$$

$$J_l(\Phi_l) = \tilde{\nu}_l(v) f_l, \quad \text{for } l \geq 1, \quad (14)$$

where  $m_0$  and  $T$  are the mass and temperature of the background neutrals. The binary collision frequency  $\nu_l(v)$  is given by,

$$\frac{\nu_l(v)}{N} = 2\pi v \int_0^{2\pi} \sigma(v, \theta) [1 - P_l(\cos \theta)] \sin \theta d\theta, \quad (15)$$

and the structure-modified collision frequency  $\tilde{\nu}_l(v)$  is:

$$\frac{\tilde{\nu}_l(v)}{N} = 2\pi v \int_0^{2\pi} \Sigma(v, \theta) [1 - P_l(\cos \theta)] \sin \theta d\theta, \quad (16)$$

where  $\Sigma(v, \theta)$  represents the structure modified differential cross-section:

$$\Sigma(v, \theta) = \sigma(v, \theta) S \left( \frac{2m_e v}{\hbar} \sin \frac{\theta}{2} \right), \quad (17)$$

which incorporates interference effects via the static structure factor  $S(q)$ , with  $q = \frac{2m_e v}{\hbar} \sin \left( \frac{\theta}{2} \right)$  representing the momentum-transfer. The structure factor  $S(q)$  encodes spatial correlations among atoms and can be obtained from the Fourier transform of the pair correlation function (Hansen and McDonald, 1976). In the dilute limit,  $S(q) \rightarrow 1$ , and the expressions reduce to those for uncorrelated binary scattering. The extension to liquid mixtures is discussed further in Section 4.2.

### 3.2.2 Modifications to the scattering potential

In addition to interference effects, the electron scattering process in dense fluids is profoundly influenced by the collective response of the surrounding medium. Two primary contributions must be considered: first, the screening of the long-range polarization potential of the focus atom by neighboring atoms, and second, the direct contribution of those surrounding atoms to the total potential experienced by the electron. Figure 3 depicts these contributions. These effects fundamentally alter the effective interaction potential and, consequently, the transport properties of electrons in liquids.

In an isolated atom, the potential felt by a nearby electron comprises a static component, governed by the ground-state electron-nucleus interaction, and a polarization term arising from the induced multipole moments within the atom. In a liquid environment, this picture becomes more complex. While the central or “focus” atom still polarizes in response to the external electron, neighboring atoms

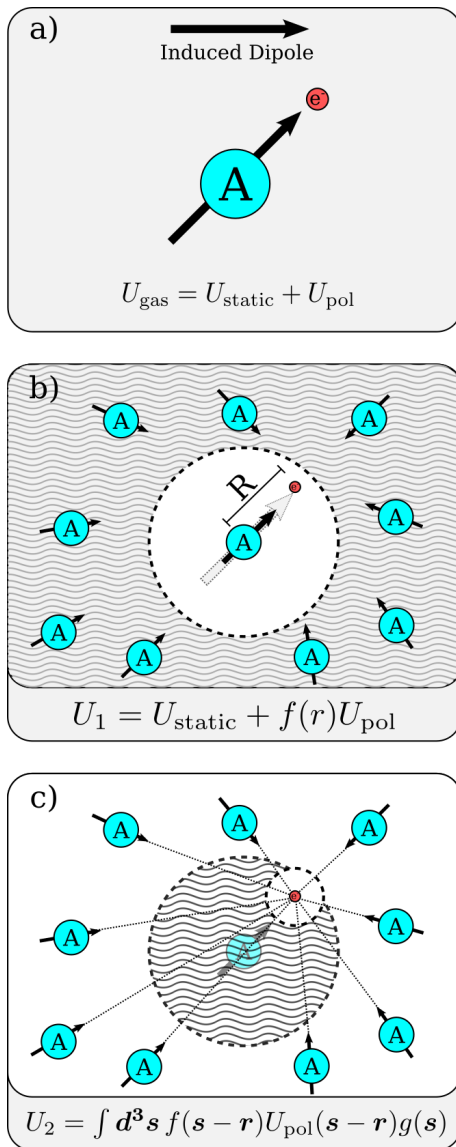


**Figure 3.** Schematic representation of the various components of the screening of the electron–atom potential in a liquid environment. (a) Gas phase potential is a combination of the static interaction potential  $U_{\text{static}}$  and the polarisation component  $U_{\text{pol}}$ . (b) Interaction potential  $U_1$  associated with the ‘focus atom’ is a combination of  $U_{\text{static}}$  and the polarisation potential screened by the surrounding atoms. (c) Interaction potential  $U_2$  associated with the surrounding atoms. Here  $r$  is the position of the electron and  $s$  the position of surrounding atoms. (Source: Reproduced from White et al. (2018), with the permission of IOP Publishing.)

also develop induced dipoles. These surrounding dipoles typically oppose the dipole moment of the focus atom, effectively screening the long-range polarization interaction. This phenomenon results

in a net reduction in the attractive polarization component of the electron–atom potential.

To quantify this screening, Lekner (1967) introduced a self-consistent screening function  $f(r)$ , which accounts for the average influence of the surrounding atomic configuration. The function satisfies the integral equation:

$$f(r) = 1 - \pi N \int_0^\infty ds \frac{g(s)}{s^2} \int_{|r-s|}^{r+s} dt \frac{\alpha_d(t) f(t) \theta(r, s, t)}{t^2}, \quad (18)$$

where  $r$  is the distance of the electron from the focus atom,  $N$  is the number density,  $g(s)$  is the pair-correlator, and  $\alpha_d$  is the dipole polarizability. The geometric factor  $\theta(r, s, t)$  arises from the transformation to bipolar coordinates and is given by:

$$\theta(r, s, t) = \frac{3(s^2 + t^2 - r^2)(s^2 + r^2 - t^2)}{2s^2 + (r^2 + t^2 - s^2)}. \quad (19)$$

In the asymptotic limit of  $r \rightarrow \infty$ , the screening function approaches the well-known Lorentz screening factor (Lekner, 1967):

$$f_L = \left[ 1 + \frac{8}{3} \pi N \alpha_d(r \rightarrow \infty) \right]^{-1}, \quad (20)$$

recovering the expected behavior in weakly interacting systems.

Beyond screening, the surrounding medium also contributes directly to the potential landscape through long-range interactions with neighboring atoms. The total effective scattering potential  $U_{\text{eff}}$  is thus composed of two terms:

$$U_{\text{eff}}(r) = U_1(r) + U_2(r), \quad (21)$$

where  $U_1(r) = U_{\text{static}}(r) + f(r)U_{\text{pol}}(r)$  is the screened potential of the focus atom, and  $U_2(r)$  accounts for the averaged potential contribution from all other atoms in the bulk. This second term

is obtained via:

$$U_2(r) = \frac{2\pi N}{r} \int_0^\infty dt t U_1(t) \int_{|r-t|}^{r+t} ds g(s). \quad (22)$$

The effective and potential components for LAr are shown in Figure 4. These modifications imply that the electron is never truly in a free space environment, i.e., the scattering potential extends throughout the medium. As a result, the use of free-particle plane waves as boundary conditions becomes invalid. Instead, one typically assumes that each atom resides within a finite spherical region, or “scattering cell,” of radius  $r_m$ , beyond which the potential is treated as approximately constant.

Different criteria have been used to define this matching radius  $r_m$ . Atrazhev and collaborators adopted the Wigner–Seitz construction, taking  $r_m = (4\pi N/3)^{-1/3}$  as the average interatomic spacing (Atrazhev and Timoshkin, 1996, 1998; Atrazhev et al., 1995). In contrast, Lekner (1967) proposed defining  $r_m$  as the first turning point of the effective potential, where  $\frac{d}{dr} U_{eff}(r_m) = 0$ . At this location, the potential is flat and the electron no longer experiences significant net forces from the surrounding medium. For the LAr case shown in Figure 4, the value of  $r_m \approx 4.3 a_0$ , which is comparable to Wigner–Seitz diameter of  $\approx 4.2 a_0$ . We also note that  $r_m \approx \frac{2}{3} \sigma_{core}$  i.e.,  $r_m$  is larger than half of the minimal interatomic separation  $\sigma_{core}$ .

Lekner introduced a shift  $V_0$  to the effective total potential such that  $U_{eff}(r_m) + V_0 = 0$ , ensuring that the potential vanishes beyond the matching radius, simplifying the application of asymptotic boundary conditions in partial wave expansions. An alternative approach, used in more recent work (Boyle et al., 2015, 2016; White et al., 2018), involves calculating the scattering phase shifts directly at  $r_m$ . This avoids artificial shifts in the potential and more accurately captures the available energy states within the liquid, especially near the conduction band minimum.

The quantity  $V_0$ , referred to as the background energy or conduction band minimum of the liquid, plays a central role in defining the energy

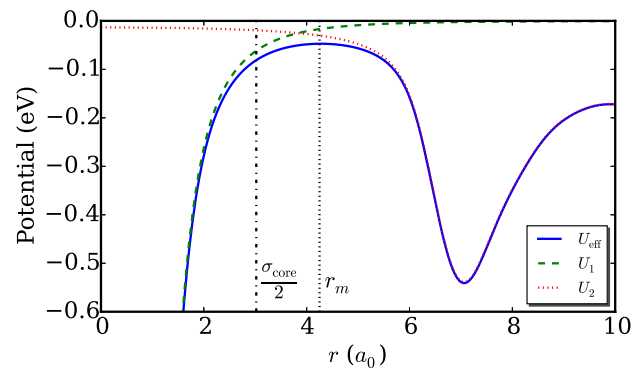


**Figure 4.** Plots of the total effective potential  $U_{eff}$  felt by an electron when colliding with one atom in the liquid. Also shown are the components,  $U_1$  and  $U_2$ , which represent the direct potential of the atom and the contribution of the remaining atoms in the bulk, respectively. The dashed vertical lines at  $\sigma_{core}/2$  and  $r_m$  indicate the hard-core exclusion radius and the proposed collisional sphere, respectively. Note that effects of exchange are not represented in this figure. (Source: Reproduced from Boyle et al. (2015), with the permission of AIP Publishing.)

scale for electron transport. Analogous to the band structure in solids, it sets the zero-point energy for delocalized electrons in the liquid. Numerous methods have been developed to estimate  $V_0$ , both theoretically (Springett et al., 1967; Hernandez, 1991; Nazin and Shikin, 2005; Yakubov and Khrapak, 1982; Nieminen et al., 1980) and experimentally (Evans and Findley, 2010; Evans et al., 2015).

These modifications to the scattering potential are essential for accurate modeling of electron transport in dense media. They determine not only the magnitude and energy dependence of scattering cross-sections but also the reference energy scale against which all transport properties, such as mobility, diffusion, and drift energy, are defined.

### 3.2.3 Example transport calculations: electrons in liquid Ar

To illustrate the practical application of the *ab initio* framework described in the previous sections, we now consider electron transport in LAr (Boyle

et al., 2015). The same methodology, with minor adaptations, has been successfully extended to other systems, including electron transport in LXe (Boyle et al., 2016), liquid krypton (White et al., 2018), and positron transport in liquid helium (Cocks et al., 2020).

At low reduced electric field strengths (typically below a few Townsends), elastic scattering dominates, and the modifications to the scattering potential and coherent effects described earlier become particularly significant. Figure 5 presents the momentum-transfer cross-sections for electron-argon scattering in both the gas and liquid phases, elucidating the separate roles of coherence and the potential modifications. For validation, the dilute gas-phase results are compared with the benchmark data of Buckman et al. (2000), which represent a synthesis of high-quality experimental measurements and theoretical predictions. The agreement confirms the accuracy of the underlying electron-argon interaction potential and the reliability of the solution technique employed.

Notably, the influence of screening and the liquid environment significantly alters the cross-section profile. In the gas phase, a pronounced Ramsauer minimum is evident, reflecting a reduced probability of momentum-transfer at specific electron energies. However, in the liquid phase, this feature is suppressed due to the screening of the polarization potential by surrounding atoms. As a result, the cross-section becomes nearly energy-independent at low incident energies, a hallmark of scattering in dense fluids. The inclusion of coherent scattering further reduces the momentum-transfer cross-section in the low-energy regime. At higher energies, where the electron's de Broglie wavelength is much shorter than the interatomic spacing, the effects of coherence and screening diminish, and the liquid-phase cross-section asymptotically approaches its gas-phase counterpart.

Figure 6 shows the calculated drift velocity and characteristic energy for electrons in LAr as functions of the reduced electric field. These

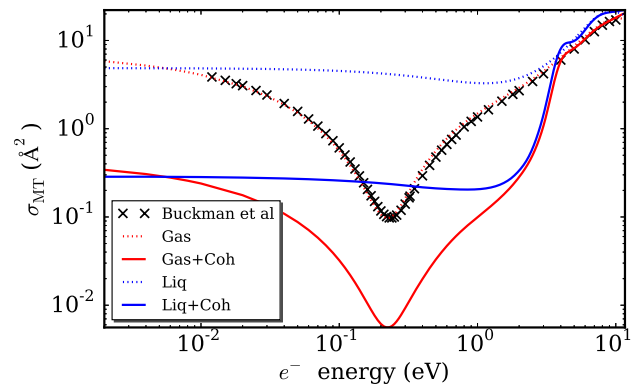


**Figure 5.** The momentum-transfer cross-sections in the gas-phase (Gas) and liquid-phase (Liq) and their modifications when coherent scattering effects are included (+Coh). The recommended transfer cross-section of Buckman et al. (2000) for a dilute gas is a combination of experimental measurements and theoretical calculations. (Source: Reproduced from Boyle et al. (2015), with the permission of AIP Publishing.)

transport properties were obtained using the cross-sections derived from the *ab initio* framework and solved via the multi-term BE formalism described in Section 3.1. For comparison, selected experimental measurements are included to validate the model. The results clearly demonstrate that applying gas-phase cross-sections scaled by density is insufficient to capture the correct transport behavior in liquids. While the gas-phase potential accurately describes transport in dilute conditions, it fails to account for the dense-medium effects that dominate in the liquid state.

Importantly, the separate impacts of coherent scattering and the potential modifications are highlighted. Coherent scattering alone is sufficient to bring the drift velocity into the correct order of magnitude. However, it overestimate the characteristic energy, further increasing the discrepancy with experimental liquid data. When combined with the potential modifications, the transport properties closely match the experimental observations, underscoring the necessity of accounting for both effects simultaneously to achieve quantitative agreement.

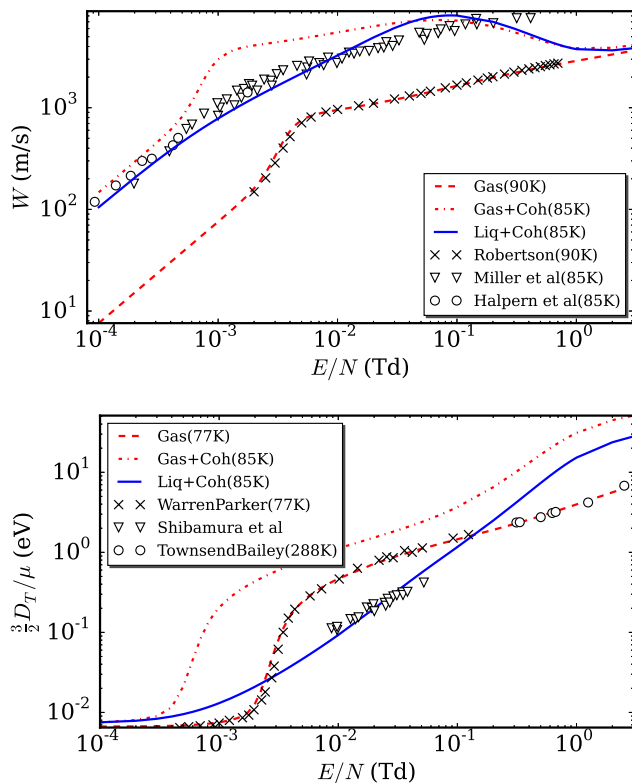


**Figure 6.** Comparison of the measured drift velocities  $W$  (top) and characteristic energies  $\frac{3}{2} D_T / \mu$  (bottom) in gaseous and liquid argon, with those calculated from the various approximations to the cross-sections. Experimental data—Ar: Robertson (1977) at 90 K; Miller et al. (1968) at 85 K; Halpern et al. (1967) at 85 K; Warren and Parker (1962) at 77 K; Townsend and A. (1922) at 288 K; Shibamura et al. (1979) at an unmeasured liquid temperature. The various approximations used are: gas phase only cross-sections (Gas), gas phase cross-sections with coherent scattering (Gas+Coh), and liquid-phase cross-sections with coherent scattering effects (Liq+Coh). The results have been calculated using the full differential cross-section and results are converged multi-term values. (Source: Reproduced from Boyle et al. (2015), with the permission of AIP Publishing.)

These results highlight the strength of the *ab initio* modeling approach in reproducing transport behavior in liquids, without the need for empirical tuning. They also emphasize the inadequacy of using gas-phase data alone in high-density regimes, and the importance of including medium-induced modifications to the scattering process in any predictive transport framework.

### 3.2.4 Inelastic scattering

While elastic scattering dominates low-energy electron transport in noble liquids, inelastic processes become increasingly relevant near and above excitation thresholds. At temperatures just below the melting point, the reflection spectrum of LXe closely resembles that of solid xenon, though the exciton lines in the liquid are shifted to lower energies and broadened due to increased structural disorder (Beaglehole, 1965).

These shifts have been traced to changes in the band gap, i.e., the energy difference between the uppermost valence band and the lowest conduction band, which decreases with increasing temperature and density (Steinberger and Asaf, 1973). This behavior is attributed to the movement of band edges as the lattice dilates. Notably, the position of excitonic features in LXe correlates linearly with the fluid's density, suggesting that interatomic distances, rather than long-range order, primarily determine the excitonic energy levels.

Spectroscopic studies have revealed several intermediate excitons in LXe, with characteristics of both Frenkel and Wannier excitons for  $n = 1$ . Prominent excitonic bands appear at approximately 8.3 eV, 9.5 eV, and 10.3 eV (Beaglehole, 1965; Asaf and Steinberger, 1971; Laporte and Steinberger, 1977; Laporte et al., 1980; Reininger et al., 1983). The first two excitonic bands have parentage in the atomic transitions  $6s(3/2)_1^0$  ( $5p^5 6s$  [ $K=3/2$ ]) at about 8.44 eV, and  $6s'(1/2)_1^0$  ( $5p^5 6s$  [ $K=1/2$ ]) at about 9.57 eV, respectively. The third peak arises from the two neighboring bands which correspond to  $5d(3/2)_1^0$  ( $5p^5 5d$  [ $K=3/2$ ]) at about 10.40 eV and  $7s(3/2)_1^0$ . For instance the intermediate exciton at 9.5 eV may be identified both as the  $^1P_1$  Frenkel exciton and as the  $n = 1$  member of the  $[\Gamma(1/2)]$  series in the Wannier notation (Laporte and Steinberger, 1977; Laporte et al., 1980). Similarly, the intermediate exciton at 8.3 eV is associated both with the  $^3P_1$  exciton in the Frenkel scheme, and as the  $n = 1$  member of the  $[\Gamma(3/2)]$  Wannier exciton series.

Higher-order excitons, such as the  $n = 2$  member of the  $[\Gamma(3/2)]$  series, have also been observed, albeit with much weaker spectral features (Asaf and Steinberger, 1971, 1974; Laporte et al., 1980). In addition to excitonic lines, broadened and shifted atomic excitation features have been identified in the reflection spectra, particularly near 8.3 eV, where they overlap with excitonic transitions (Asaf and Steinberger, 1971; Laporte and Steinberger, 1977; Laporte et al., 1980).

The emergence of excitonic features in the reflection spectrum is strongly density-dependent. Studies show that excitonic lines begin to appear at densities significantly below the liquid state, with no abrupt transition from the “dense gas” to “liquid” regime, even along continuous thermodynamic paths where the entire system is a single-phase one (Laporte and Steinberger, 1977; Laporte et al., 1980). Exciton formation requires local clusters of atoms large enough to contain an exciton within its characteristic radius. Where this condition is not met, only broadened atomic transitions are observed. Both the excitonic lines and the perturbed atomic excitations exist in LXe, and they both contribute to energy losses of quasifree electrons in the conduction band, complicating first-principles model development.

Photoconductivity measurements provide a complementary insight. The conduction band minimum in LXe, corresponding to the  $\Gamma(3/2)$  gap, has been determined to lie at 9.22 eV (Asaf and Steinberger, 1974), in agreement with estimates based on density changes upon melting. A dip in the photoconductivity spectrum near 9.45 eV coincides with the  $n = 1$  member of  $[\Gamma(1/2)]$  exciton, suggesting competition between optical excitation and free-carrier generation. At higher energies, up to about 10.0 eV no further structure in the photoconductivity spectra has been observed (Asaf and Steinberger, 1974).

The evolution of the photoconductivity spectra of fluid xenon with increasing density from  $10^{21}$  atoms/cm<sup>3</sup> up to the triple point density has been thoroughly investigated by Reininger et al.

(1983). It has been found that the photoconductivity threshold decreases with increasing density. Its extrapolation to zero density yields 11.10 eV which is the difference between the energy minimum of the  $\text{Xe}_2^+$  molecular ion and the ground-state energy of the xenon atom. It has been observed that there is a decrease in photocurrent at about 10.32 eV, where a reflectivity maximum has been observed Reininger et al. (1983). While for the interband transitions the electrons and holes become quasifree, this discrete bound state likely has alternative decay channels like luminescence, which reduces the measured photocurrent at the line. At higher liquid densities and in the solid phase, the discrete 9.45 eV reflection peak appears as a pronounced dip in the photoconductivity spectrum.

Despite the wealth of spectroscopic data, theoretical treatments of inelastic scattering in noble liquids remain limited. In early transport studies of LXe and LAr (Garland et al., 2018b; Simonović et al., 2019), inelastic collisions were treated approximately, due to the lack of reliable cross-section data for exciton formation, perturbed atomic excitations, and interband transitions in the liquid phase. Crucially, the fraction of clusters that support exciton formation versus those contributing only perturbed atomic transitions remains unknown, especially for optically forbidden transitions that still contribute to inelastic energy loss for conduction-band electrons.

To address this, Garland et al. (2018b) and Simonović et al. (2019) approximated the interband excitation cross-sections in LXe and LAr using gas-phase electron impact ionization cross-sections, adjusted to match the known liquid band gaps. Similarly, excitonic and atomic excitation cross-sections were approximated using those of isolated atoms. Wannier excitons with  $n > 1$  were omitted, as their parentage lies beyond atomic excited states, and only weak spectral signatures (e.g., the  $n = 2$  exciton at 9.0 eV) have been observed (Asaf and Steinberger, 1971).

For the case of LXe, Simonović et al. (2019) systematically explored four scenarios for including

inelastic excitations in their transport model, using the cross-section set from Hayashi (2003):

1. No excitations included, i.e., assuming purely elastic and ionizing collisions.
2. Only excitations below the band gap included, consistent with the approach in Garland et al. (2018b) for LAr.
3. First four excitations from the Hayashi cross-section set included, to account for the optically allowed excitation which leads to the pronounced dip in the photoconductivity spectra of LXe at about 9.45 eV as well as one optically forbidden excitation which has a slightly lower threshold.
4. All excitations in the Hayashi set included, extending coverage to features up to 10.3 eV.

For each scenario, the ionization coefficient in LXe was calculated and compared to experimental data from Derenzo et al. (1974), and is shown in Figure 7. Interestingly, the first two experimental points matched best with the first scenario (no excitation), while the remaining data aligned closely with the fourth scenario (all excitations included).

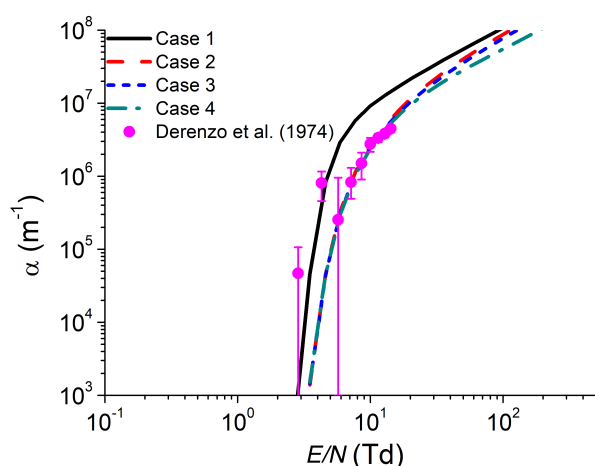


**Figure 7.** Comparison of the ionization coefficient  $\alpha$  for electrons in LXe calculated by Simonović et al. (2019) for four different treatments of inelastic collisions (see text for details) with the experimental measurements of Derenzo et al. (1974).

However, it is important to note that the experimental ionization data are limited to relatively low reduced electric fields, well below those used in advanced detectors. Thus, while the fourth case shows good agreement at low fields, it is uncertain whether these approximations remain valid at higher fields. At elevated energies, the detailed structure of the conduction band and the exact inelastic scattering dynamics may play a more prominent role, requiring a more rigorous theoretical treatment.

### 3.3 Electron self-trapping

In liquid-phase systems, electron transport is not always governed solely by scattering and diffusion. Under certain conditions, excess electrons may become transiently localized in the medium due to spontaneous density fluctuations. This phenomenon, known as electron self-trapping, results in the formation of localized states, such as bubbles or solvated electron configurations, that significantly alter the transport dynamics (Nieminen et al., 1980; Maris, 2003; Rumbach et al., 2015; Abel, 2013; Gopalakrishnan et al., 2016).

The driving mechanism behind self-trapping lies in the nature of the electron–atom interaction in noble liquids. These interactions are typically dominated by short-range repulsion, resulting in a positive background potential  $V_0(N) > 0$ , where  $N$  is the local atomic density. An electron can lower its free energy by migrating into regions of reduced density, where the value of  $V_0$  is lower. If the density depression is large enough, the energetic gain from a reduced potential energy can outweigh both the kinetic energy cost of localization and the mechanical work needed to expand the local cavity (Borghesani et al., 1992; Hernandez, 1991). In such cases, a metastable localized state may be formed. These states are weakly bound and have been observed in both theoretical studies and experimental measurements of atomic liquids (Borghesani, 2006).

Borghesani (2006) proposed a phenomenological model for mobility in systems exhibiting self-trapping, treating the total electron mobility as a weighted average of contributions from two populations: free (delocalized) electrons and localized electrons trapped in density fluctuations. The mobility of the free electrons is computed using a heuristic kinetic model, while the contribution from localized electrons is modeled using hydrodynamic descriptions of bubble transport. Although this approach qualitatively reproduces observed trends, it struggled to match absolute mobility values, primarily because the assumption of a single, well-defined localized state is an oversimplification. In reality, liquid systems support a broad distribution of fluctuation sizes and configurations, each contributing differently to the transport properties.

To address these limitations, more sophisticated approaches have been developed. Cocks and White (2016) performed *ab initio* calculations of the probability that an electron scatters into a low-density region and becomes trapped. Their model accounts for both the formation and energetic stability of these localized states and provides a physically grounded framework for studying electron localization in liquids.

Further progress was made by Stokes and collaborators (Stokes et al., 2016), who introduced a generalized BE capable of describing the interplay between localized and delocalized electron populations. Their framework incorporates scattering into and out of density fluctuations, allowing for both trapping and detrapping processes to be treated self-consistently. This hybrid transport model provides a more complete picture of electron dynamics in systems where localization phenomena are non-negligible.

Overall, electron self-trapping represents a key departure from conventional gas-phase transport behavior and introduces rich physics into the study of dense, disordered systems. Accurate treatment of this effect is essential for modeling electron mobility in noble liquids, particularly under

low-field or low-temperature conditions where fluctuations are more prominent and localization becomes more probable.

## 4 APPLICATIONS AND CHALLENGES FOR LIQUID DETECTORS

While much progress has been made in understanding the fundamental physics of electron transport in noble liquids, practical applications in detector design introduce additional complexities. In this section, we examine selected challenges and applications relevant to noble-liquid detectors, with a focus on scintillation and luminescence, doped and mixed-liquid systems, and charge transport across gas-liquid interfaces.

### 4.1 Scintillation and Luminescence

Studies of ionisation, scintillation, and luminescence in noble gases and liquids, particularly in LAr and LXe, play a vital role in the development of modern detector technologies (González-Díaz et al., 2018; Bonivento and Terranova, 2024). When a charged particle traverses a noble liquid, energy dissipation occurs via ionization, excitation, and the generation of sub-excitation electrons. The average energy loss per ionization event slightly exceeds the ionization potential or the energy for the interband transition, as it encompasses multiple ionisation events. Notably, the average ionization energy is lower in the liquid phase compared to the gas, implying more efficient ionization. Among noble liquids, LXe exhibits a lower energy cost per ion pair than LAr, resulting in a higher ionization yield. The liberated electrons then drift and diffuse under an applied electric field, enabling both calorimetric and spatial reconstruction in TPC detectors (Aprile and Baudis, 2010).

Scintillation, the emission of light following atomic or molecular excitation, plays a central role in signal formation. More broadly, luminescence includes all photon emission processes (scintillation among them) arising from energy deposition and subsequent relaxation of excited states. In the context of liquid noble gases, these terms are often

used interchangeably, and we refer to all prompt light emission as scintillation.

In LAr and LXe, scintillation is predominantly driven by the formation and subsequent de-excitation of dimers, also known as excimers, i.e., transient, bound states formed when an excited atom ( $\text{Ar}^*$  or  $\text{Xe}^*$ ) interacts with ground-state atoms. These excimers exist in singlet and triplet configurations, which de-excite by emitting vacuum ultraviolet (VUV) photons: approximately 128 nm in LAr and 178 nm in LXe. Time-resolved spectroscopy confirms this mechanism, showing distinct fast and slow scintillation components that correspond to singlet and triplet state lifetimes (Kubota et al., 1978; Hitachi et al., 1983; Segreto, 2021). Further experimental evidence includes the dependence of scintillation yield and timing on factors such as electric field intensity, particle type, and energy deposition (Doke et al., 2002; Doke, 2006). These observations are consistent with theoretical models that describe the formation and decay of excimers.

Direct de-excitation of excited atoms also contributes to scintillation, though to a lesser extent. For example, in LXe, isolated  $\text{Xe}^*$  atoms can emit photons upon returning to the ground state. However, in the dense liquid environment, this pathway is suppressed in favor of excimer ( $\text{Xe}_2^*$ ) formation via collisions between excited and ground-state xenon atoms. Although the direct de-excitation of excited LXe atoms plays a relatively minor role in the scintillation process compared to the excimer mechanism, it does contribute to the overall luminescence.

To model these processes quantitatively, accurate rate coefficients for inelastic collisions, such as atomic excitations and interband transitions, are required. Figure 8 illustrates rate coefficients computed using MC simulations and electron scattering cross-sections from Simonović et al. (2019). At low reduced fields,  $E/N$ , excitation and interband transitions are negligible. However, as  $E/N$  increases beyond 20 Td, the interband transition rate becomes dominant. The computed

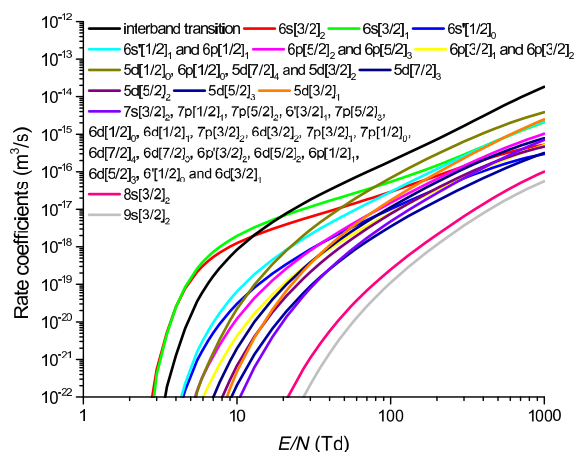


**Figure 8.** Rate coefficients for interband transition and electronic excitations in LXe as a function of  $E/N$ . See text for details.

rate coefficients are smooth and featureless, reflecting the threshold-like onset of inelastic processes as electrons gain sufficient energy. These results are essential for refining empirical simulation tools such as NEST (Szydagis et al., 2011, 2021, 2025). In addition, the rate coefficients for various inelastic processes are required as input for the fluid modeling of discharges in LXe.

Doping is a powerful technique for enhancing detector performance. For example, introducing trace amounts of LXe into LAr shifts the emission spectrum from 128 nm to 175–178 nm. This shift improves photon detection efficiency by reducing Rayleigh scattering and matching the spectral sensitivity of common photodetectors. Even at concentrations as low as a few parts per million, xenon doping can significantly increase scintillation yield by enabling energy transfer from LAr to LXe excimers (Segreto, 2021; Fields et al., 2023; Abud et al., 2024). A first step towards accurate *ab initio* modeling of doped and simple liquid mixtures is detailed in Section 4.2.

In contrast, impurities such as nitrogen, oxygen, and water vapor degrade detector performance by quenching scintillation and capturing free electrons. These species either absorb VUV photons or serve as electron scavengers, reducing both light output and charge collection. Oxygen, in particular, has a high electron affinity and is highly

disruptive to charge readout (Acciarri et al., 2010; Barrelet et al., 2002). Modeling studies have been conducted to understand impurity dynamics in LAr detectors, including their sources, transport, and removal mechanisms. To mitigate these effects, sophisticated purification systems and impurity monitoring tools, such as ultra-sensitive trace gas sensors developed for the DARKSIDE experiment, have been employed to maintain purity at sub-part-per-billion levels (Mount et al., 2012).

Overall, the interplay between excitation, ionization, and scintillation mechanisms, along with the impact of doping and impurity control, defines the performance of noble-liquid detectors. Accurate modeling of these processes, supported by both experimental data and advanced simulations, remains critical for optimizing detector response and enabling precision measurements in neutrino and dark matter experiments.

## 4.2 Electron transport in doped and mixture systems

The ECFA DRD roadmap Colaleo et al. (2021) highlighted the potential benefits of using liquid mixtures and dopants as a detector medium. For instance, doping LAr with small concentrations of LXe has been shown to enhance charge amplification by over two orders of magnitude (Kim et al., 2002), offering a promising route for improved detector performance (Segreto, 2021; Fields et al., 2023; Abud et al., 2024). As discussed in Section 4.1, even trace amounts of LXe in LAr reducing Rayleigh scattering, matches the spectral sensitivity of common photodetectors, and enables energy transfer from LAr to LXe excimers.

In Section 3.2, we introduced the formalism for coherent elastic scattering in pure single-component liquids. Extending this framework to mixtures involves generalizing the collision operator to account for multiple species. In the case of a binary mixture (e.g., a doped LAr–LXe system), the coherent elastic collision operator generalizes

to (Boyle et al., 2024):

$$J_0(\Phi_0) = \frac{m_e}{m_a v^2} \left[ v \nu_1^a(v) \left( v \Phi_l + \frac{k_b T}{m_e} \frac{d}{dv} \Phi_0 \right) \right] + \frac{m_e}{m_b v^2} \left[ v \nu_1^b(v) \left( v \Phi_l + \frac{k_b T}{m_e} \frac{d}{dv} \Phi_l \right) \right], \quad (23)$$

$$J_l(\Phi_l) = \tilde{\nu}_l(v) \Phi_l, \quad \text{for } l \geq 1, \quad (24)$$

where  $\nu_l^a(v)$  and  $\nu_l^b(v)$  are the usual Legendre components of the binary collision frequencies for each species:

$$\frac{\nu_l^{a,b}(v)}{x_{a,b} N} = 2\pi v \int_0^{2\pi} \sigma_{a,b}(v, \theta) [1 - P_l(\cos \theta)] \sin \theta d\theta. \quad (25)$$

The structure-modified collision frequency  $\tilde{\nu}_l(v)$  is now calculated from the combined differential cross-section:

$$\Sigma(v, \theta) = \sigma_a(v, \theta) S_{aa}(K) + \sigma_b(v, \theta) S_{bb}(K) + 2\sqrt{\sigma_a(v, \theta) \sigma_b(v, \theta)} S_{ba}(K). \quad (26)$$

where  $K = \frac{2m_e v}{\hbar} \sin \frac{\theta}{2}$ , and  $S_{aa}$ ,  $S_{bb}$  and  $S_{ab}$  are the partial static structure factors describing intra- and inter-species correlations (see Boyle et al. (2024); Hansen and McDonald (1976) for details). In the dilute limit where  $K$  is large, the structure factors approach their respective mole fractions ( $S_{aa}(K) \rightarrow x_a$ ,  $S_{bb}(K) \rightarrow x_b$  and  $S_{ab}(K) \rightarrow 0$ ) and the usual binary scattering results are recovered, as required. The formalism also correctly reduces to the single-species case when  $\sigma_b \rightarrow \sigma_a$ , i.e.,  $S_{aa} + 2S_{ab} + S_{bb} \rightarrow S_a$ , where  $S_a$  represents the structure factor of the pure fluid.

The static structure factors and pair distribution functions required in these calculations can be obtained via molecular dynamics or MC simulations (van Gunsteren and Berendsen, 1990; Lindgård, 1994; Wedberg et al., 2011). However, for hard-sphere liquids, an analytic solution is available from the Percus–Yevick approximation (Percus and Yevick, 1958; Lebowitz, 1964; Hiroike, 1969). For binary mixtures, the structure is fully specified by

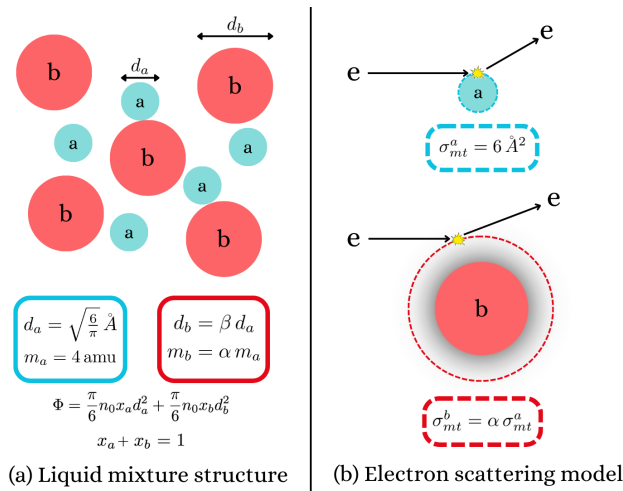


**Figure 9.** Benchmark binary system of cold ( $T = 0$  K) hard-spheres. **a)** Parameters describing the liquid mixture structure:  $d_a$  ( $d_b$ ),  $m_a$  ( $m_b$ ) and  $x_a$  ( $x_b$ ) are the hard-sphere diameter, mass and density fraction of species  $a$  (species  $b$ ), respectively.  $\Phi$  is the total packing factor,  $N$  is the total number density. **b)** Parameters describing the electron scattering:  $\sigma_{mt}^a$  ( $\sigma_{mt}^b$ ) is the momentum-transfer cross-section for electron scattering from species  $a$  (species  $b$ ), and  $\sigma_0^a - \sigma_l^a = \sigma_{mt}^a$  ( $\sigma_0^b - \sigma_l^b = \sigma_{mt}^b$ ) is constant for all  $l$ . (Source: Reproduced from Boyle et al. (2024), with the permission of IOP Publishing.)

ratio of hard-sphere diameters of the two species  $\beta = \frac{d_b}{d_a}$ , the diameter and density fraction of species  $a$  ( $d_a$ ,  $x_a$ ), and the total packing fraction  $\Phi$ :

$$\Phi = \frac{\pi}{6} N x_a d_a^2 + \frac{\pi}{6} N x_b d_b^2. \quad (27)$$

where  $x_b = 1 - x_a$ , and  $N$  is the total number density. These parameters define the extent of spatial correlation within the mixture and strongly influence electron transport. We now consider the benchmark model introduced in Boyle et al. (2024), shown in Figure 9.

Figure 10 illustrates the structure-modified collision components  $\Sigma_0 - \Sigma_l$  for three different compositions: pure species  $a$  ( $x_a = 1$ ), pure species  $b$  ( $x_a = 0$ ), and a 50:50 mixture ( $x_a = 0.5$ ). Similar to the pure liquid case, the structure-modified profiles exhibit oscillations around the constant binary scattering value and show significant suppression of momentum-transfer

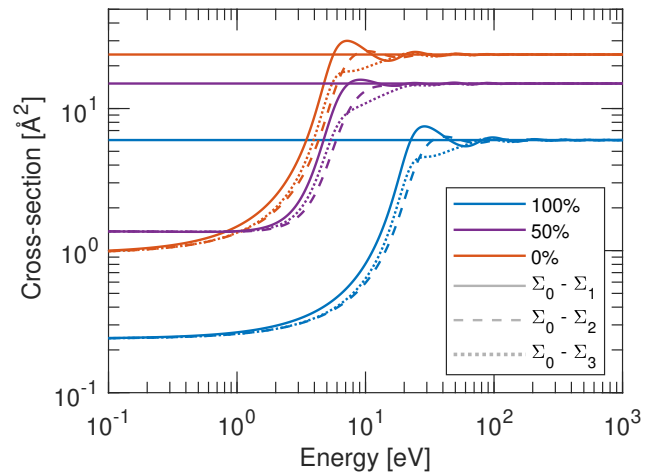


**Figure 10.** Scattering cross-section variation with electron energy for the binary hard-sphere mixture given in Figure 9. Partial cross-sections  $\Sigma_0 - \Sigma_l$  vs energy are given for varying percentages of species  $a$ , and with parameters  $\Phi = 0.4$ ,  $\alpha = \frac{\sigma_b}{\sigma_a} = 4$ ,  $\beta = \frac{d_b}{d_a} = 2$ . Horizontal lines represent the (constant) binary-scattering limit cross-sections. (Source: Reproduced from Boyle et al. (2024), with the permission of IOP Publishing.)

at low energies. Interestingly, at energies near 0.1 eV, the 50:50 mixture profile exceeds those of both pure systems, indicating non-linear mixing behavior in the cross-sections.

These effects are directly reflected in the calculated transport coefficients. Figure 11 shows the variation of drift velocity  $W$ , mean energy  $\epsilon$ , and reduced diffusion coefficients  $ND_L$  and  $ND_T$ , as functions of the reduced electric field. The results are shown for two packing fractions ( $\Phi = 0.2$  and  $\Phi = 0.4$ ) with  $\beta = 2$  and  $\alpha = \beta^2 = 4$ . Large variations spanning orders of magnitude are observed across different mixture compositions. Notably, at the higher packing density ( $\Phi = 0.4$ ), the transport coefficients for the 50:50 mixture fall outside the range bounded by the two pure species, a behavior not seen at lower density ( $\Phi = 0.2$ ). This non-linearity underscores the importance of particle correlations in dense mixtures and their impact on transport properties.

As demonstrated in Boyle et al. (2024), even modest amounts of dopant or secondary species

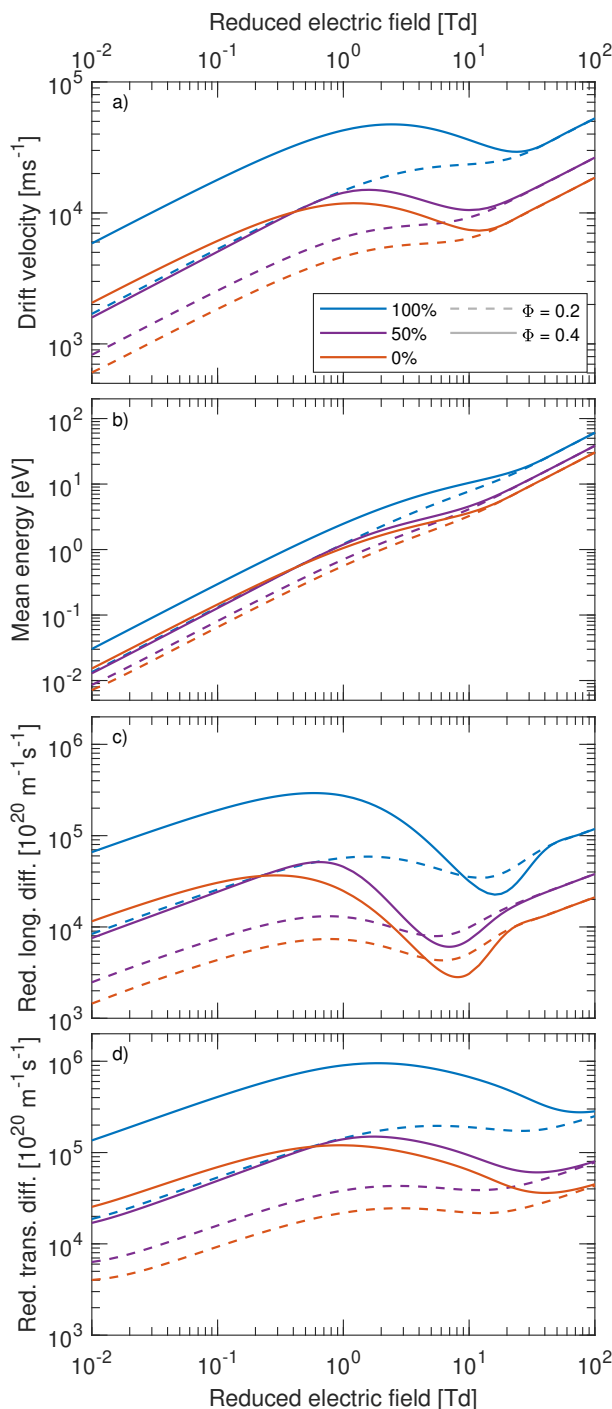


**Figure 11.** Transport properties for varying mixture percentage of species *a*. The parameters of species *a* and *b* are set according to the model given in Figure 9, with  $\alpha = \frac{\sigma_b}{\sigma_a} = 4$  and  $\beta = \frac{d_b}{d_a} = 2$ . **a)** Drift velocity, **b)** Mean energy, **c)** Reduced longitudinal diffusion coefficient, **d)** Reduced transverse diffusion coefficient. (Source: Reproduced from Boyle et al. (2024), with the permission of IOP Publishing.)

can dramatically alter electron transport in noble liquid systems, sometimes enhancing and other times suppressing mobility and diffusion compared to the pure fluids. This opens new possibilities for tuning detector media by carefully selecting admixture compositions to optimize signal response, timing, or gain.

Although coherent elastic scattering dominates at low electron energies, a complete description of transport in mixtures also requires accounting for how dopants affect polarization screening and bulk potential contributions. Extending the framework developed in Section 3.2.2 to multi-component systems is a subject of ongoing work, and will be essential for predictive modeling of next-generation doped noble-liquid detectors.

### 4.3 Electron transport across the gas-liquid interface

Dual-phase TPCs take advantage of both the liquid and gas phases of noble elements, and are central to many state-of-the-art detectors Colaleo et al. (2021); Baudis (2024). In these systems, a well-defined gas-liquid interface is intrinsic to the detector geometry, typically formed by maintaining the liquid at its boiling point through controlled vapor-condensation mechanisms.

In a typical dual-phase detector, ionization electrons generated in the liquid drift under a modest electric field until they reach the interface. At this boundary, they are extracted into the vapor phase, where higher field strengths are used to generate secondary scintillation light or avalanche multiplication via amplification grids. The efficiency and fidelity of this extraction process are crucial for detector sensitivity, timing resolution, and energy reconstruction. However, the gas-liquid interface introduces several physical complexities that are not present in homogeneous systems.

One significant complication is the likely accumulation of surface charge at the interface in both the longitudinal and transverse directions, relative to the extracting field. Such charge buildup may lead to distortions of the local electric field,

inhibit electron extraction, or produce spurious signals, especially in large-scale detectors where small distortions can impact performance over long drift distances. Moreover, the microscopic structure of the interface, which is shaped by atomic-scale density gradients and thermal fluctuations, further complicates the prediction of electron behavior near this region.

Accurately modeling electron transport across the gas–liquid boundary requires more than simply adding together the transport models from each phase. While simplified approaches often treat the interface as a sharp boundary layer with idealized transfer conditions, a more complete and physically consistent treatment must account for the continuous variation in density, potential energy, and scattering environment that electrons encounter as they approach and cross the interface.

A promising step in this direction comes from recent work by Garland et al. (2018a), who modeled the interface as a smooth density gradient characterized by an equilibrium profile spanning the two phases. Key to their approach was the relation of the spatial variation in  $V_0$ , the quasi-free electron energy, to a varying effective electric potential which through the gradient presents as a spatially inhomogeneous effective electric field. This effective field may then functionally act to inhibit electron extraction across the interface from LAr or LXe to gas, or conversely accelerate electron transport from gas into liquid. This approach is supported by molecular dynamics and MC simulations, which show that noble liquids such as LAr and LXe exhibit finite-thickness interfacial layers with well-defined thermodynamic properties. Early studies (Chapela et al., 1977; Trokhymchuk and Alexandre, 1999) employed Lennard-Jones potentials to simulate noble gas interactions and were able to reproduce key interfacial properties, including the surface tension, equilibrium vapor and liquid densities, and the interfacial width.

These simulations provide critical inputs for transport modeling, especially for defining the spatial variation of scattering cross-sections,

background potential energy, and local electron density in the interfacial region. Incorporating this information into kinetic, fluid or MC models enables a more accurate and continuous treatment of electron transport from liquid to gas. It also provides a path towards predicting extraction efficiencies, timing characteristics, and possible sources of noise originating from interfacial phenomena. As dual-phase detectors continue to scale in size and complexity, a deeper understanding of interfacial electron dynamics grounded in molecular simulation and kinetic theory will be essential for ensuring the performance and reliability of future experiments.

## 5 SUMMARY

In this work, we have provided an overview of the experimental and theoretical landscape of electron transport in noble liquids, with a particular focus on applications to liquid xenon and liquid argon time projection chambers. We reviewed key swarm measurements of electron mobility and diffusion, drawing from studies spanning several decades, and highlighted the importance of these measurements for validating transport models used in modern detectors. These measurements reveal consistent trends but also emphasize the need for high-purity systems and standardized reporting of experimental conditions.

We examined the state-of-the-art in modeling low-energy electron transport in dense media, with particular emphasis on multi-term solutions to the Boltzmann equation. Central to this theoretical framework are the use of structure-modified elastic scattering cross-sections and *ab initio* interaction potentials that incorporate polarization screening and bulk medium effects. Our analysis highlighted the limitations of gas-phase scaling and reinforces the need for liquid-specific scattering models that account for collective effects and self-localization of electrons. Inelastic processes, while less well characterized, are also critical, particularly exciton formation and interband transitions, which remain

active areas of research due to the lack of reliable liquid-phase cross-sections.

For next-generation noble-liquid detectors, an accurate understanding of excitation processes, and consequently, scintillation and luminescence, is essential. While progress has been made, especially in modeling excimers, predicting light yields in varying field and impurity conditions remains a significant challenge. Recent proposals involving doped and mixed noble liquids open new opportunities for tuning the optical and electronic properties of the detector medium. Furthermore, the transport of electrons across the gas-liquid interface also remains an important frontier, where improved modeling can reduce systematic uncertainties and guide interface engineering in dual-phase detectors. Emerging machine learning techniques and improved datasets offer promising tools for tackling each of these complex problems.

Looking to the future, as noble-liquid detectors continue to scale to kilotonne and even multi-kilotonne active masses, the demands on predictive transport models become more acute. Precise modeling of diffusion, recombination, and ionization dynamics is essential not only for preserving signal fidelity over meter-scale drift lengths, but also for the design of optimized detector geometries, electric field configurations, and readout systems. In this context, advances in *ab initio* theory, data-driven modeling, machine learning, and targeted measurements will be critical for achieving predictive, reliable descriptions of electron transport in noble liquids, capable of spanning the full range of operating conditions from sub-Td reduced fields to high-field extraction regimes.

## CONFLICT OF INTEREST STATEMENT

The authors declare that the research was conducted in the absence of any commercial or financial relationships that could be construed as a potential conflict of interest.

## AUTHOR CONTRIBUTIONS

GB: Conceptualization, Data curation, Formal analysis, Investigation, Methodology, Project administration, Software, Validation, Visualization, Writing – original draft, Writing – review & editing. NG: Conceptualization, Data curation, Formal analysis, Investigation, Methodology, Project administration, Software, Validation, Visualization, Writing – original draft, Writing – review & editing. DM: Conceptualization, Data collection, Data curation, Formal analysis, Investigation, Software, Validation, Visualization, Writing – original draft, Writing – review & editing. IS: Data curation, Formal analysis, Investigation, Methodology, Software, Validation, Visualization, Writing – original draft, Writing – review & editing. IS: Data curation, Formal analysis, Investigation, Methodology, Software, Validation, Visualization, Writing – original draft, Writing – review & editing. DB: Data curation, Formal analysis, Investigation, Methodology, Software, Validation, Visualization, Writing – review & editing. SD: Data curation, Formal analysis, Funding acquisition, Investigation, Methodology, Software, Supervision, Validation, Visualization, Writing – original draft, Writing – review & editing. RW: Conceptualization, Formal analysis, Funding acquisition, Investigation, Resources, Supervision, Writing – review & editing.

## FUNDING

DM and RW gratefully acknowledge the financial support of the Australian Research Council (ARC) through the Discovery Projects Scheme (DP220101480 and DP190100696). IS, DB, and SD acknowledge the support of the Ministry of Science, Technological Development and Innovations of the Republic of Serbia and the Institute of Physics Belgrade.

## ACKNOWLEDGMENTS

The authors wish to thank Bob McEachran for his unrivaled expertise, scattering calculations,

and continued support for the development of electron-liquid transport models. The authors would also like to thank Diego Ramírez García for valuable discussions on TPC operation and analysis. The authors acknowledge the use of ChatGPT (GPT-4-turbo, April 9th 2024 update) by OpenAI. The prompt *Proofread the following scientific manuscript for spelling and grammar errors. Ensure consistency in tense, technical terminology, and punctuation. Maintain the formal academic tone, and revise the text where needed to ensure a consistent use of first-person plural narration (e.g., “we show”, “our results”). Do not rephrase unnecessarily—keep the original style and structure wherever possible* was employed for the final draft. The authors have checked the factual accuracy of the output.

## DATA AVAILABILITY STATEMENT

The datasets for the experimental measurements considered in this study can be found at [www.github.com/jcu-transport-physics/liquid-transport-data](https://www.github.com/jcu-transport-physics/liquid-transport-data).

## REFERENCES

- Aalbers, J., Akerib, D. S., Akerlof, C. W., Al Musalhi, A. K., Alder, F., Alqahtani, A., et al. (2023). First Dark Matter Search Results from the LUX-ZEPLIN (LZ) Experiment. *Physical Review Letters* 131, 041002. doi:10.1103/PhysRevLett.131.041002
- Abel, B. (2013). Hydrated interfacial ions and electrons. *Annual review of physical chemistry* 64, 533–552
- Abi, B., Abud, A. A., Acciarri, R., Acero, M., Adamov, G., Adamowski, M., et al. (2020). First results on ProtoDUNE-SP liquid argon time projection chamber performance from a beam test at the CERN Neutrino Platform. *Journal of Instrumentation* 15, P12004. doi:10.1088/1748-0221/15/12/P12004
- Abratenko, P., Alrashed, M., An, R., Anthony, J., Asaadi, J., Ashkenazi, A., et al. (2021a). Cosmic Ray Background Rejection with Wire-Cell LArTPC Event Reconstruction in the MicroBooNE Detector. *Physical Review Applied* 15, 064071. doi:10.1103/PhysRevApplied.15.064071
- Abratenko, P., An, R., Anthony, J., Asaadi, J., Ashkenazi, A., Balasubramanian, S., et al. (2021b). Measurement of the longitudinal diffusion of ionization electrons in the MicroBooNE detector. *Journal of Instrumentation* 16, P09025. doi:10.1088/1748-0221/16/09/P09025
- Abud, A. A., Abi, B., Acciarri, R., Acero, M. A., Adames, M., Adamov, G., et al. (2024). Doping liquid argon with xenon in protodune single-phase: effects on scintillation light. *Journal of Instrumentation* 19, P08005
- Acciarri, R., Antonello, M., Baibussinov, B., Baldo-Ceolin, M., Benetti, P., Calaprice, F., et al. (2010). Oxygen contamination in liquid argon: combined effects on ionization electron charge and scintillation light. *Journal of Instrumentation* 5, P05003
- Albert, J. B., Barbeau, P. S., Beck, D., Belov, V., Breidenbach, M., Brunner, T., et al. (2017). Measurement of the drift velocity and transverse diffusion of electrons in liquid xenon with the EXO-200 detector. *Physical Review C* 95, 025502
- Aprile, E., Agostini, F., Alfonsi, M., Althueser, L., Amaro, F. D., Antochi, V. C., et al. (2019). XENON1T dark matter data analysis: Signal and background models and statistical inference. *Physical Review D* 99, 112009. doi:10.1103/PhysRevD.99.112009
- Aprile, E., Arisaka, K., Arneodo, F., Askin, A., Baudis, L., Behrens, A., et al. (2012). The XENON100 dark matter experiment. *Astroparticle Physics* 35, 573–590. doi:10.1016/j.astropartphys.2012.01.003
- Aprile, E. and Baudis, L. (2010). Liquid noble gases. In *Particle Dark Matter*, ed. G. Bertone (Cambridge University Press). 413–436. doi:10.1017/cbo9780511770739.022

- Asaf, U. and Steinberger, I. T. (1971). Wannier excitons in liquid xenon. *Physics Letters A* 34, 207–208. doi:https://doi.org/10.1016/0375-9601(71)90831-0
- Asaf, U. and Steinberger, I. T. (1974). Photoconductivity and electron transport parameters in liquid and solid xenon. *Phys. Rev. B* 10, 4464–4468. doi:10.1103/PhysRevB.10.4464
- Atrazhev, V., Iakubov, I., and Pogosov, V. (1995). Evolution of the ramsauer effect on scattering of electrons in liquids. *Physics Letters A* 204, 393–398
- Atrazhev, V. M. and Iakubov, I. T. (1981). Hot electrons in non-polar liquids. *Journal of Physics C: Solid State Physics* 14, 5139. doi:10.1088/0022-3719/14/33/021
- Atrazhev, V. M. and Timoshkin, I. V. (1996). Electron scattering by a cut-off atomic potential: Application to electron properties in atomic liquids. *Phys. Rev. B* 54, 11252–11260. doi:10.1103/PhysRevB.54.11252
- Atrazhev, V. M. and Timoshkin, I. V. (1998). Transport of electrons in atomic liquids in high electric fields. *IEEE Transactions on Dielectrics and Electrical Insulation* 5, 450–457. doi:10.1109/94.689434
- Barrelet, E., Andrieu, B., Babaev, A., Banas, E., Bederede, D., Biddulph, P., et al. (2002). A purity monitoring system for the h1 liquid argon calorimeter. *Nuclear Instruments and Methods in Physics Research Section A: Accelerators, Spectrometers, Detectors and Associated Equipment* 490, 204–222
- Baudis, L. (2024). Dual-phase xenon time projection chambers for rare-event searches. *Philosophical Transactions of the Royal Society A* 382, 20230083
- Baudis, L., Biondi, Y., Bismark, A., Cimental Chávez, A. P., Cuenca-García, J. J., Franchi, J., et al. (2023). Electron transport measurements in liquid xenon with Xenoscope, a large-scale DARWIN demonstrator. *The European Physical Journal C* 83, 717. doi:10.1140/epjc/s10052-023-11823-1
- Baudis, L., Biondi, Y., Capelli, C., Galloway, M., Kazama, S., Kish, A., et al. (2018). A dual-phase xenon TPC for scintillation and ionisation yield measurements in liquid xenon. *The European Physical Journal C* 78, 351. doi:10.1140/epjc/s10052-018-5801-5
- Baur, D., Bismark, A., Brown, A., Dierle, J., Fischer, H., Glade-Beucke, R., et al. (2023). The XeBRA platform for liquid xenon time projection chamber development. *Journal of Instrumentation* 18, T02004. doi:10.1088/1748-0221/18/02/T02004
- Beaglehole, D. (1965). Reflection studies of excitons in liquid and solid xenon. *Phys. Rev. Lett.* 15, 551–553. doi:10.1103/PhysRevLett.15.551
- Beever, Z., Caratelli, D., Fava, A., Pietropaolo, F., Stocker, F., and Zettlemoyer, J. (2024). TRANSLATE - a Monte Carlo simulation of electron transport in liquid argon. *Computer Physics Communications* 297, 109056. doi:10.1016/j.cpc.2023.109056
- Boer, D., Verhoeven, S., Graef, W., Carbone, E., and van Dijk, J. (2023). Lxcat 3: A novel data platform for low temperature plasma physics. In *International Conference on Phenomena in Ionized Gases XXXV, ICPIG XXXV ; Conference date: 09-07-2023 Through 14-07-2023*. 165
- Boltzmann, L. (1872). Weitere Studien über das Wärmegleichgewicht unter Gasmolekülen. *Wiener Berichte* 66, 275–370
- Bonivento, W. M. and Terranova, F. (2024). The science and technology of liquid argon detectors. *Rev. Mod. Phys.* 96, 045001. doi:10.1103/RevModPhys.96.045001
- Borghesani, A. F. (2006). Electron and ion transport in dense rare gases. *IEEE Transactions on Dielectrics and Electrical Insulation* 13, 492–502. doi:10.1109/TDEI.2006.1657960
- Borghesani, A. F. (2014). Electron swarm experiments in dense rare gases: A review. *The European Physical Journal D* 68, 62
- Borghesani, A. F. (2021). Accurate electron drift mobility measurements in moderately dense helium gas at several temperatures. *Atoms* 9, 52

- Borghesani, A. F., Bruschi, L., Santini, M., and Torzo, G. (1988). Electron mobility in neon at high densities. *Physical Review A* 37, 4828–4835. doi:10.1103/PhysRevA.37.4828
- Borghesani, A. F. and Santini, M. (1994). Density and field dependence of excess electron mobility in high-density noble gases. In *Linking the Gaseous and Condensed Phases of Matter: The Behavior of Slow Electrons* (Springer). 259–279
- Borghesani, A. F., Santini, M., and Lamp, P. (1992). Excess electron mobility in high-density argon gas. *Physical Review A* 46, 7902–7909. doi:10.1103/PhysRevA.46.7902
- Boyle, G. J., Garland, N. A., McEachran, R. P., Mirihana, K. A., Robson, R. E., Sullivan, J. P., et al. (2024). Electron scattering and transport in simple liquid mixtures. *Journal of Physics B: Atomic, Molecular and Optical Physics* 57, 015202. doi:10.1088/1361-6455/ad1d35
- Boyle, G. J., McEachran, R. P., Cocks, D. G., Brunger, M. J., Buckman, S. J., Dujko, S., et al. (2016). Ab initio electron scattering cross-sections and transport in liquid xenon. *Journal of Physics D: Applied Physics* 49, 355201. doi:10.1088/0022-3727/49/35/355201
- Boyle, G. J., McEachran, R. P., Cocks, D. G., and White, R. D. (2015). Electron scattering and transport in liquid argon. *The Journal of Chemical Physics* 142, 154507. doi:10.1063/1.4917258
- Boyle, G. J., Stokes, P. W., Robson, R. E., and White, R. D. (2023). Boltzmann's equation at 150: Traditional and modern solution techniques for charged particles in neutral gases. *The Journal of Chemical Physics* 159, 024306. doi:10.1063/5.0153973
- Boyle, G. J., Tattersall, W. J., Cocks, D. G., McEachran, R. P., and White, R. D. (2017). A multi-term solution of the space-time Boltzmann equation for electrons in gases and liquids. *Plasma Sources Science and Technology* 26, 024007. doi:10.1088/1361-6595/aa51ef
- Braglia, G. L. and Dallacasa, V. (1982). Theory of electron mobility in dense gases. *Phys. Rev. A* 26, 902–914. doi:10.1103/PhysRevA.26.902
- Bruschi, L., Mazzi, G., and Santini, M. (1972). Localized Electrons in Liquid Neon. *Physical Review Letters* 28, 1504–1506. doi:10.1103/PhysRevLett.28.1504
- Buckley, E., Campanella, M., Carugno, G., Cattadori, C., Gonidec, A., Muñoz, R., et al. (1989). A study of ionization electrons drifting over large distances in liquid argon. *Nuclear Instruments and Methods in Physics Research Section A: Accelerators, Spectrometers, Detectors and Associated Equipment* 275, 364–372. doi:10.1016/0168-9002(89)90710-9
- Buckman, S., Cooper, J., Elford, M., Inokuti, M., Itikawa, Y., and Tawara, H. (2000). Photon and electron interactions with atoms, molecules and ions. *Numerical Data and Functional Relationships in Science and Technology, Heidelberg*
- Burnett, D. (1935). The distribution of velocities in a slightly non-uniform gas. *Proceedings of the London Mathematical Society* 39, 385–430
- Burnett, D. (1936). The distribution of molecular velocities and the mean motion in a non-uniform gas. *Proceedings of the London Mathematical Society* 40, 382–435
- Carbone, E., Graef, W., Hagelaar, G., Boer, D., Hopkins, M. M., Stephens, J. C., et al. (2021). Data needs for modeling low-temperature non-equilibrium plasmas: The lxcat project, history, perspectives and a tutorial. *Atoms* 9. doi:10.3390/atoms9010016
- Champion, C., Le Loirec, C., and Stosic, B. (2012). Epotran: a full-differential monte carlo code for electron and positron transport in liquid and gaseous water. *International journal of radiation biology* 88, 54–61
- Chapela, G. A., Saville, G., Thompson, S. M., and Rowlinson, J. S. (1977). Computer simulation of a gas-liquid surface. part 1. *Journal of the Chemical Society, Faraday Transactions 2: Molecular and Chemical Physics* 73, 1133–1144
- Chapman, S. and Cowling, T. G. (1970). *The mathematical theory of non-uniform gases: an account of the kinetic theory of viscosity, thermal*

- conduction and diffusion in gases (Cambridge university press)
- Cocks, D., McEachran, R., Boyle, G., Cheng, E., and White, R. (2020). Positron scattering and transport in liquid helium. *Journal of Physics B: Atomic, Molecular and Optical Physics* 53, 225201
- Cocks, D. and White, R. (2016). Fluctuation capture in non-polar gases and liquids. *arXiv preprint arXiv:1602.07834*
- Cohen, E. and Thirring, W. (1973). *The Boltzmann Equation* (Springer)
- Cohen, M. H. and Lekner, J. (1967). Theory of hot electrons in gases, liquids, and solids. *Phys. Rev.* 158, 305–309. doi:10.1103/PhysRev.158.305
- Colaleo, A., Ropelewski, L., Dehmelt, K., Liberti, B., Titov, M., Veloso, J., et al. (2021). *The 2021 ECFA Detector Research and Development Roadmap* (CERN). doi:10.17181/CERN.XDPL.W2EX
- Davidson, N. and Larsh, A. E. (1950). Conductivity Pulses Induced in Insulating Liquids by Ionizing Radiations. *Physical Review* 77, 706–711. doi:10.1103/PhysRev.77.706
- Derenzo, S. E., Mast, T. S., Zaklad, H., and Muller, R. A. (1974). Electron avalanche in liquid xenon. *Phys. Rev. A* 9, 2582–2591. doi:10.1103/PhysRevA.9.2582
- Doke, T. (1981). Fundamental properties of liquid argon, krypton and xenon as radiation detector media. *Portugaliae Physica* 12, 9–48
- Doke, T. (1982). Recent developments of liquid xenon detectors. *Nuclear Instruments and Methods in Physics Research* 196, 87–96. doi:10.1016/0029-554X(82)90621-8
- Doke, T. (2006). Scintillation of liquid xenon and its application to nuclear radiation detectors. *IEEE Transactions on Dielectrics and Electrical Insulation* 13, 640–649. doi:10.1109/TDEI.2006.1657979
- Doke, T., Hitachi, A., Kikuchi, J., Masuda, K., Okada, H., and Shibamura, E. (2002). Absolute scintillation yields in liquid argon and xenon for various particles. *Japanese Journal of Applied Physics* 41, 1538. doi:10.1143/JJAP.41.1538
- Dujko, S., White, R. D., and Petrović, Z. L. (2008). Monte carlo studies of non-conservative electron transport in the steady-state townsend experiment. *Journal of Physics D: Applied Physics* 41, 245205
- Eibl, R., Lamp, P., and Buschhorn, G. (1990). Measurement of electron mobility in liquid and critical argon at low electric-field strengths. *Physical Review B* 42, 4356–4362. doi:10.1103/PhysRevB.42.4356
- Emfietzoglou, D., Karava, K., Papamichael, G., and Moscovitch, M. (2003). Monte carlo simulation of the energy loss of low-energy electrons in liquid water. *Physics in Medicine & Biology* 48, 2355
- Emfietzoglou, D., Papamichael, G., and Nikjoo, H. (2017). Monte carlo electron track structure calculations in liquid water using a new model dielectric response function. *Radiation research* 188, 355–368
- Engelhardt, A. G. and Phelps, A. V. (1963). Elastic and inelastic collision cross sections in hydrogen and deuterium from transport coefficients. *Phys. Rev.* 131, 2115–2128. doi:10.1103/PhysRev.131.2115
- Engelhardt, A. G., Phelps, A. V., and Risk, C. G. (1964). Determination of momentum transfer and inelastic collision cross sections for electrons in nitrogen using transport coefficients. *Phys. Rev.* 135, A1566–A1574. doi:10.1103/PhysRev.135.A1566
- Evans, C. M. and Findley, G. (2010). Energy of the conduction band in near critical point fluids. *Physics Research International* 2010
- Evans, C. M., Krynski, K., Streeter, Z., and Findley, G. L. (2015). Energy of the quasi-free electron in H<sub>2</sub>, D<sub>2</sub>, and O<sub>2</sub>: Probing intermolecular potentials within the local Wigner-Seitz model. *The Journal of Chemical Physics* 143, 224303. doi:10.1063/1.4936627
- Fields, D., Gibbons, R., Gold, M., McFadden, N., Elliott, S. R., and Massarczyk, R. (2023). Understanding the enhancement of scintillation light in xenon-doped liquid argon. *Nuclear Instruments and Methods in Physics*

- Research Section A: Accelerators, Spectrometers, Detectors and Associated Equipment* 1046, 167707
- Frost, L. S. and Phelps, A. V. (1962). Rotational excitation and momentum transfer cross sections for electrons in H<sub>2</sub> and N<sub>2</sub> from transport coefficients. *Phys. Rev.* 127, 1621–1633. doi:10.1103/PhysRev.127.1621
- Garland, N., Boyle, G., Cocks, D., and White, R. (2018a). Approximating the nonlinear density dependence of electron transport coefficients and scattering rates across the gas–liquid interface. *Plasma Sources Science and Technology* 27, 024002
- Garland, N., Simonović, I., Boyle, G., Cocks, D., Dujko, S., and White, R. (2018b). Electron swarm and streamer transport across the gas–liquid interface: a comparative fluid model study. *Plasma Sources Science and Technology* 27, 105004
- González-Díaz, D., Monrabal, F., and Murphy, S. (2018). Gaseous and dual-phase time projection chambers for imaging rare processes. *Nuclear Instruments and Methods in Physics Research Section A: Accelerators, Spectrometers, Detectors and Associated Equipment* 878, 200–255
- Gopalakrishnan, R., Kawamura, E., Lichtenberg, A., Lieberman, M., and Graves, D. (2016). Solvated electrons at the atmospheric pressure plasma–water anodic interface. *Journal of Physics D: Applied Physics* 49, 295205
- Gushchin, E. M., Kruglov, A. A., and Obodovskii, I. M. (1982). Electron dynamics in condensed argon and xenon. *Soviet Journal of Experimental and Theoretical Physics* 55, 650
- Halpern, B., Lekner, J., Rice, S. A., and Gomer, R. (1967). Drift Velocity and Energy of Electrons in Liquid Argon. *Physical Review* 156, 351–352. doi:10.1103/PhysRev.156.351
- Hansen, J.-P. and McDonald, I. R. (1976). *Theory of simple liquids* (Academic press)
- Hayashi, M. (2003). *Bibliography of electron and photon cross sections with atoms and molecules published in the 20th century. Xenon*. Tech. rep., National Inst. for Fusion Science
- Hernandez, J. P. (1991). Electron self-trapping in liquids and dense gases. *Rev. Mod. Phys.* 63, 675–697. doi:10.1103/RevModPhys.63.675
- Hiroike, K. (1969). Ornstein-zernike relation for a fluid mixture with direct correlation functions of finite range. *Journal of the Physical Society of Japan* 27, 1415–1421. doi:10.1143/JPSJ.27.1415
- Hitachi, A., Takahashi, T., Funayama, N., Masuda, K., Kikuchi, J., and Doke, T. (1983). Effect of ionization density on the time dependence of luminescence from liquid argon and xenon. *Phys. Rev. B* 27, 5279–5285. doi:10.1103/PhysRevB.27.5279
- Hogenbirk, E., Decowski, M., McEwan, K., and Colijn, A. (2018). Field dependence of electronic recoil signals in a dual-phase liquid xenon time projection chamber. *Journal of Instrumentation* 13, P10031–P10031. doi:10.1088/1748-0221/13/10/P10031
- Huang, S. S.-S. and Freeman, G. R. (1978). Electron mobilities in gaseous, critical, and liquid xenon: Density, electric field, and temperature effects: Quasilocalization. *The Journal of Chemical Physics* 68, 1355–1362. doi:10.1063/1.435954
- Huang, S. S.-S. and Freeman, G. R. (1981). Electron transport in gaseous and liquid argon: Effects of density and temperature. *Physical Review A* 24, 714–724. doi:10.1103/PhysRevA.24.714
- Huxley, L. G. H. and Crompton, R. W. (1974). *Diffusion and drift of electrons in gases* (John Wiley & Sons)
- Iakubov, I.-T. and Khrapak, A. (1982). Self-trapped states of positrons and positronium in dense gases in liquids. *Reports on Progress in Physics* 45, 697
- Jetly, V. and Chaudhury, B. (2021). Extracting electron scattering cross sections from swarm data using deep neural networks. *Machine Learning: Science and Technology* 2, 035025. doi:10.1088/2632-2153/abf15a

- Jörg, F., Cichon, D., Eurin, G., Höttsch, L., Marrodán Undagoitia, T., and Rupp, N. (2022). Characterization of alpha and beta interactions in liquid xenon. *The European Physical Journal C* 82, 361. doi:10.1140/epjc/s10052-022-10259-3
- [Dataset] Kalinin, A. M., Gonidec, A., Schinzel, D., and Potrebennikov, Yu. K. (1996). Temperature and Electric Field Strength Dependence of Electron Drift Velocity in Liquid Argon.
- Kim, J., Dardin, S., Jackson, K., Kadel, R., Kadyk, J., Peskov, V., et al. (2002). Studies of electron avalanche behavior in liquid argon. *IEEE Transactions on Nuclear Science* 49, 1851–1856. doi:10.1109/TNS.2002.801490
- Kondo, K. and Tagashira, H. (1990). Evolution equation and transport coefficients defined by arrival-time spectra of swarms. *Journal of Physics D: Applied Physics* 23, 1175. doi:10.1088/0022-3727/23/9/007
- Kubota, S., Hishida, M., and Raun, J. (1978). Evidence for a triplet state of the self-trapped exciton states in liquid argon, krypton and xenon. *Journal of Physics C: Solid State Physics* 11, 2645. doi:10.1088/0022-3719/11/12/024
- Kumar, K. (1966). Polynomial expansions in kinetic theory of gases. *Annals of physics* 37, 113–141
- Kumar, K. (1967). The Chapman-Enskog solution of the Boltzmann equation: A reformulation in terms of irreducible tensors and matrices. *Australian Journal of Physics* 20, 205–252
- Kumar, K., Skullerud, H., and Robson, R. E. (1980). Kinetic theory of charged particle swarms in neutral gases. *Australian Journal of Physics* 33, 343–448
- Lamp, P. and Buschhorn, G. (1994). Electron transport in fluid argon in combined electric and magnetic fields. *Physical Review B* 50, 16824–16834. doi:10.1103/PhysRevB.50.16824
- Laporte, P. and Steinberger, I. T. (1977). Evolution of excitonic bands in fluid xenon. *Phys. Rev. A* 15, 2538–2544. doi:10.1103/PhysRevA.15.2538
- Laporte, P., Subtil, J. L., Asaf, U., Steinberger, I. T., and Wind, S. (1980). Intermediate and wannier excitons in fluid xenon. *Phys. Rev. Lett.* 45, 2138–2140. doi:10.1103/PhysRevLett.45.2138
- Lebowitz, J. L. (1964). Exact solution of generalized Percus-Yevick equation for a mixture of hard spheres. *Phys. Rev.* 133, A895–A899. doi:10.1103/PhysRev.133.A895
- Lekner, J. (1967). Motion of electrons in liquid argon. *Phys. Rev.* 158, 130–137. doi:10.1103/PhysRev.158.130
- Lemmon, E. (2025). *Thermophysical Properties of Fluid Systems* (Gaithersburg MD, 20899: Eds. P.K. Linstrom and W.G. Mallard, National institute of Standards and Technology). Retrieved March 3, 2025
- Li, Y., Tsang, T., Thorn, C., Qian, X., Diwan, M., Joshi, J., et al. (2016). Measurement of longitudinal electron diffusion in liquid argon. *Nuclear Instruments and Methods in Physics Research Section A: Accelerators, Spectrometers, Detectors and Associated Equipment* 816, 160–170. doi:10.1016/j.nima.2016.01.094
- Lindgård, P. A. (1994). Computer simulation of the structure factor. In *Computer Simulation Studies in Condensed-Matter Physics VII*, eds. D. P. Landau, K. K. Mon, and H.-B. Schüttler (Berlin, Heidelberg: Springer Berlin Heidelberg), 69–82
- Liu, J. (2022). The first results of PandaX-4T. *International Journal of Modern Physics D* 31, 2230007. doi:10.1142/S0218271822300075
- Loffhagen, D. and Winkler, R. (1996). Multi-term treatment of the temporal electron relaxation in He, Xe and plasmas. *Plasma Sources Science and Technology* 5, 710
- Maeda, K. and Makabe, T. (1994). Time-dependent rf swarm transport by direct numerical procedure of the Boltzmann equation. *Japanese Journal of Applied Physics* 33, 4173. doi:10.1143/JJAP.33.4173
- Makabe, T. and Petrovic, Z. L. (2006). *Plasma Electronics: Applications in Microelectronic Device Fabrication* (CRC Press)
- Malkin, M. S. and Schultz, H. L. (1951). Electron Mobilities in Liquid Argon. *Physical Review* 83, 1051–1052. doi:10.1103/PhysRev.83.1051.2

- Maris, H. (2003). Properties of electron bubbles in liquid helium. *Journal of low temperature physics* 132, 77–95
- Mehnaz, Yang, L., Zou, Y., Da, B., Mao, S., Li, H., et al. (2020). A comparative study on Monte Carlo simulations of electron emission from liquid water. *Medical Physics* 47, 759–771. doi:10.1002/mp.13913
- Miller, L. S., Howe, S., and Spear, W. E. (1968). Charge Transport in Solid and Liquid Ar, Kr, and Xe. *Physical Review* 166, 871–878. doi:10.1103/PhysRev.166.871
- Morgan, W. (1991). The feasibility of using neural networks to obtain cross sections from electron swarm data. *IEEE Transactions on Plasma Science* 19, 250–255. doi:10.1109/27.106821
- Mount, B. J., Serfling, G. L., Sun, Y., Thompson, J. D., Durben, D., and Keeter, K. J. (2012). Developing a 0.1 ppb trace gas impurity sensor for noble liquid-based direct dark matter detectors. In *Proceedings of the South Dakota Academy of Science*. vol. 91, 159
- Muccignat, D. L., Boyle, G. G., Garland, N. A., Stokes, P. W., and White, R. D. (2024). An iterative deep learning procedure for determining electron scattering cross-sections from transport coefficients. *Machine Learning: Science and Technology* 5, 015047. doi:10.1088/2632-2153/ad2fed
- Nazin, S. and Shikin, V. (2005). Minimum energy of a free electron in inert gases. *Journal of Experimental and Theoretical Physics Letters* 82, 236–240
- Ness, K. and Robson, R. E. (1986). Velocity distribution function and transport coefficients of electron swarms in gases. ii. moment equations and applications. *Physical Review A* 34, 2185
- Nieminen, R. M., Välimaa, I., Manninen, M., and Hautojärvi, P. (1980). Density-functional theory of positronium and electron bubbles in helium fluids. *Phys. Rev. A* 21, 1677–1686. doi:10.1103/PhysRevA.21.1677
- Nishikawa, M., Holroyd, R. A., and Preses, J. M. (2007). Mobility of electrons in supercritical krypton: Role of density fluctuations. *The Journal of Chemical Physics* 127, 014504. doi:10.1063/1.2746870
- Njoya, O., Tsang, T., Tarka, M., Fairbank, W., Kumar, K. S., Rao, T., et al. (2020). Measurements of electron transport in liquid and gas Xenon using a laser-driven photocathode. *Nuclear Instruments and Methods in Physics Research Section A: Accelerators, Spectrometers, Detectors and Associated Equipment* 972, 163965
- [Dataset] Park, R., Scheiner, B. S., and Zammit, M. C. (2023). ThunderBoltz: An Open-Source DSMC-based Boltzmann Solver for Plasma Transport, Chemical Kinetics, and 0D Plasma Modeling
- Penetrante, B., Bardsley, J., and Pitchford, L. (1985). Monte carlo and boltzmann calculations of the density gradient expanded energy distribution functions of electron swarms in gases. *Journal of Physics D: Applied Physics* 18, 1087
- Percus, J. K. and Yevick, G. J. (1958). Analysis of classical statistical mechanics by means of collective coordinates. *Phys. Rev.* 110, 1–13. doi:10.1103/PhysRev.110.1
- Petrović, Z. L., Dujko, S., Marić, D., Malović, G., Nikitović, Ž., Šašić, O., et al. (2009). Measurement and interpretation of swarm parameters and their application in plasma modelling. *Journal of Physics D: Applied Physics* 42, 194002
- Petrović, Z. L., Marjanović, S., Dujko, S., Banković, A., Malović, G., Buckman, S., et al. (2014). On the use of monte carlo simulations to model transport of positrons in gases and liquids. *Applied Radiation and Isotopes* 83, 148–154
- Pitchford, L. C., O'Neil, S. V., and Rumble, J. R. (1981). Extended Boltzmann analysis of electron swarm experiments. *Phys. Rev. A* 23, 294–304. doi:10.1103/PhysRevA.23.294
- Pitchford, L. C. et al. (2017). LXCat: an open-access, web-based platform for data needed for modeling low temperature plasmas. *Plasma Processes and Polymers* 14, 1600098. doi:https://doi.org/10.1002/ppap.201600098

- Polischuk, A. Y. (1984). Theory of electron mobility in dense gases with small polarizability. *Physica B+ C* 124, 91–95
- Pruett, H. D. and Broida, H. P. (1967). Free-carrier drift-velocity studies in rare-gas liquids and solids. *Physical Review* 164, 1138–1144. doi:10.1103/PhysRev.164.1138
- Reininger, R., Asaf, U., Steinberger, I. T., Saile, V., and Laporte, P. (1983). Photoconductivity and the evolution of energy bands in fluid xenon. *Phys. Rev. B* 28, 3193–3199. doi:10.1103/PhysRevB.28.3193
- Robertson, A. (1977). Drift velocities of low energy electrons in argon at 293 and 90 K. *Australian Journal of Physics* 30, 39–50
- Robson, R. (1984). Generalized Einstein relation and negative differential conductivity in gases. *Australian journal of physics* 37, 35–44
- Robson, R. (1991). Transport phenomena in the presence of reactions: definition and measurement of transport coefficients. *Australian journal of physics* 44, 685–692
- Robson, R. and Ness, K. (1986). Velocity distribution function and transport coefficients of electron swarms in gases: spherical-harmonics decomposition of Boltzmann's equation. *Physical Review A* 33, 2068
- Robson, R. E. (1986). Physics of reacting particle swarms in gases. *The Journal of Chemical Physics* 85, 4486–4501. doi:10.1063/1.451769
- Robson, R. E., White, R. D., and Hildebrandt, M. (2017). *Fundamentals of Charged Particle Transport in Gases and Condensed Matter* (CRC Press)
- Rumbach, P., Bartels, D. M., Sankaran, R. M., and Go, D. B. (2015). The solvation of electrons by an atmospheric-pressure plasma. *Nature communications* 6, 7248
- Sakai, Y. (2007). Quasifree electron transport under electric field in nonpolar simple-structured condensed matters. *Journal of Physics D: Applied Physics* 40, R441–R452. doi:10.1088/0022-3727/40/24/R01
- Sakai, Y., Böttcher, H., and Schmidt, W. F. (1982). Excess electrons in liquid hydrogen, liquid neon, and liquid helium. *Journal of Electrostatics* 12, 89–96. doi:10.1016/0304-3886(82)90070-5
- Sakai, Y., Nakamura, S., and Tagashira, H. (1985). Drift velocity of hot electrons in liquid Ar, Kr, and Xe. *IEEE Transactions on Electrical Insulation* EI-20, 133–137. doi:10.1109/TEI.1985.348789
- Sakai, Y., Tagashira, H., and Sakamoto, S. (1977). The development of electron avalanches in argon at high  $E/N$  values. i. Monte Carlo simulation. *Journal of Physics D: Applied Physics* 10, 1035. doi:10.1088/0022-3727/10/7/010
- Schmidt, W., Illenberger, E., Khrapak, A., Sakai, Y., and Yoshino, K. (2003). Electronic conduction and breakdown in liquid helium and liquid neon. *IEEE Transactions on Dielectrics and Electrical Insulation* 10, 1012–1021. doi:10.1109/TDEI.2003.1255779
- Schmidt, W. F. (1984). Electronic conduction processes in dielectric liquids. *IEEE Transactions on Electrical Insulation* EI-19, 389–418. doi:10.1109/TEI.1984.298767
- Schnyders, H., Rice, S. A., and Meyer, L. (1965). Electron Mobilities in Liquid Argon. *Physical Review Letters* 15, 187–190. doi:10.1103/PhysRevLett.15.187
- Schnyders, H., Rice, S. A., and Meyer, L. (1966). Electron Drift Velocities in Liquefied Argon and Krypton at Low Electric Field Strengths. *Physical Review* 150, 127–145. doi:10.1103/PhysRev.150.127
- Schumann, M. (2019). Direct detection of wimp dark matter: concepts and status. *Journal of Physics G: Nuclear and Particle Physics* 46, 103003. doi:10.1088/1361-6471/ab2ea5
- Segreto, E. (2021). Properties of liquid argon scintillation light emission. *Phys. Rev. D* 103, 043001. doi:10.1103/PhysRevD.103.043001
- Shibamura, E., Takahashi, T., Kubota, S., and Doke, T. (1979). Ratio of diffusion coefficient to mobility for electrons in liquid argon. *Physical Review A* 20, 2547–2554. doi:10.1103/PhysRevA.20.2547
- Shinsaka, K., Codama, M., Srithanratana, T., Yamamoto, M., and Hatano, Y. (1988). Electron-ion recombination rate constants in gaseous,

- liquid, and solid argon. *The Journal of Chemical Physics* 88, 7529–7536. doi:10.1063/1.454317
- Sigeneger, F. and Winkler, R. (1996). Response of the electron kinetics on spatial disturbances of the electric field in nonisothermal plasmas. *Contributions to Plasma Physics* 36, 551–571
- Simonović, I., Garland, N., Bošnjaković, D., Petrović, Z. L., White, R., and Dujko, S. (2019). Electron transport and negative streamers in liquid xenon. *Plasma Sources Science and Technology* 28, 015006. doi:10.1088/1361-6595/aaf968
- Skullerud, H. R. (1968). The stochastic computer simulation of ion motion in a gas subjected to a constant electric field. *Journal of Physics D: Applied Physics* 1, 1567. doi:10.1088/0022-3727/1/11/423
- Springett, B. E., Cohen, M. H., and Jortner, J. (1967). Properties of an excess electron in liquid helium: The effect of pressure on the properties of the negative ion. *Phys. Rev.* 159, 183–190. doi:10.1103/PhysRev.159.183
- Steinberger, I. T. and Asaf, U. (1973). Band-structure parameters of solid and liquid xenon. *Phys. Rev. B* 8, 914–918. doi:10.1103/PhysRevB.8.914
- Stephens, J. (2018). A multi-term boltzmann equation benchmark of electron-argon cross-sections for use in low temperature plasma models. *Journal of Physics D: Applied Physics* 51, 125203
- Stokes, P. W., Cocks, D. G., Brunger, M. J., and White, R. D. (2020). Determining cross sections from transport coefficients using deep neural networks. *Plasma Sources Science and Technology* 29, 055009
- Stokes, P. W., Philippa, B., Cocks, D., and White, R. D. (2016). Solution of a generalized boltzmann's equation for nonequilibrium charged-particle transport via localized and delocalized states. *Phys. Rev. E* 93, 032119. doi:10.1103/PhysRevE.93.032119
- Swan, D. W. (1962). Electron Drift Velocity in Liquid Argon and Argon–Nitrogen Mixtures. *Nature* 196, 977–978. doi:10.1038/196977a0
- Szydakis, M., Balajthy, J., Block, G., Brodsky, J., Brown, E., Cutter, J., et al. (2022). A review of nest models, and their application to improvement of particle identification in liquid xenon experiments. *arXiv preprint arXiv:2211.10726*
- Szydakis, M., Balajthy, J., Block, G. A., Brodsky, J. P., Brown, E., Cutter, J. E., et al. (2025). A review of nest models for liquid xenon and an exhaustive comparison with other approaches. *Frontiers in Detector Science and Technology* 2, 1480975
- Szydakis, M., Barry, N., Kazkaz, K., Mock, J., Stolp, D., Sweany, M., et al. (2011). Nest: a comprehensive model for scintillation yield in liquid xenon. *Journal of Instrumentation* 6, P10002. doi:10.1088/1748-0221/6/10/P10002
- Szydakis, M., Block, G. A., Farquhar, C., Flesher, A. J., Kozlova, E. S., Levy, C., et al. (2021). A review of basic energy reconstruction techniques in liquid xenon and argon detectors for dark matter and neutrino physics using nest. *Instruments* 5
- Tagashira, H., Sakai, Y., and Sakamoto, S. (1977). The development of electron avalanches in argon at high e/n values. ii. Boltzmann equation analysis. *Journal of Physics D: Applied Physics* 10, 1051. doi:10.1088/0022-3727/10/7/011
- Tattersall, W. J., Cocks, D. G., Boyle, G. J., Buckman, S. J., and White, R. D. (2015). Monte Carlo study of coherent scattering effects of low-energy charged particle transport in Percus-Yevick liquids. *Physical Review E (Statistical, Nonlinear, and Soft Matter Physics)* 91, 043304. doi:10.1103/PhysRevE.91.043304
- The ICARUS Collaboration (2004). Measurement of the  $\mu$  decay spectrum with the ICARUS liquid Argon TPC. *The European Physical Journal C - Particles and Fields* 33, 233–241. doi:10.1140/epjc/s2004-01597-7
- Thieme, K. (2022). *The Low-Energy and Large-Scale Frontier of Dual-Phase Xenon Time Projection Chambers for Dark Matter Search*. Ph.D. thesis, Zurich U.

- Townsend, J. S. and A., B. V. (1922). The motion of electrons in argon. *The London, Edinburgh, and Dublin Philosophical Magazine and Journal of Science* 43, 593–600. doi:10.1080/14786442.208633916
- Trokhymchuk, A. and Alexandre, J. (1999). Computer simulations of liquid/vapor interface in lennard-jones fluids: Some questions and answers. *The Journal of chemical physics* 111, 8510–8523
- Trunec, D., Bonaventura, Z., and Nečas, D. (2006). Solution of time-dependent Boltzmann equation for electrons in non-thermal plasma. *Journal of Physics D: Applied Physics* 39, 2544
- Tskhakaya, D., Matyash, K., Schneider, R., and Taccogna, F. (2007). The Particle-In-Cell Method. *Contributions to Plasma Physics* 47, 563–594. doi:10.1002/ctpp.200710072
- van Gunsteren, W. F. and Berendsen, H. J. C. (1990). Computer simulation of molecular dynamics: Methodology, applications, and perspectives in chemistry. *Angewandte Chemie International Edition in English* 29, 992–1023. doi:https://doi.org/10.1002/anie.199009921
- Walkowiak, W. (2000). Drift velocity of free electrons in liquid argon. *Nuclear Instruments and Methods in Physics Research Section A: Accelerators, Spectrometers, Detectors and Associated Equipment* 449, 288–294. doi:10.1016/S0168-9002(99)01301-7
- Wang Chang, C. S., Uhlenbeck, G. E., and de Boer, J. (1964). *Studies in Statistical Mechanics*, vol. II (North-Holland)
- Warren, R. W. and Parker, J. H. (1962). Ratio of the diffusion coefficient to the mobility coefficient for electrons in he, ar, n<sub>2</sub>, h<sub>2</sub>, d<sub>2</sub>, co, and co<sub>2</sub> at low temperatures and low  $\frac{E}{p}$ . *Phys. Rev.* 128, 2661–2671. doi:10.1103/PhysRev.128.2661
- Wedberg, R., O'Connell, J. P., Peters, G. H., and Abildskov, J. (2011). Pair correlation function integrals: Computation and use. *The Journal of Chemical Physics* 135, 084113. doi:10.1063/1.3626799
- White, R. D., Cocks, D., Boyle, G., Casey, M., Garland, N., Konovalov, D., et al. (2018). Electron transport in biomolecular gaseous and liquid systems: theory, experiment and self-consistent cross-sections. *Plasma Sources Science and Technology* 27, 053001. doi:10.1088/1361-6595/aabdd7
- White, R. D., Robson, R., Dujko, S., Nicoletopoulos, P., and Li, B. (2009). Recent advances in the application of Boltzmann equation and fluid equation methods to charged particle transport in non-equilibrium plasmas. *Journal of Physics D: Applied Physics* 42, 194001
- White, R. D., Robson, R. E., Schmidt, B., and Morrison, M. A. (2003). Is the classical two-term approximation of electron kinetic theory satisfactory for swarms and plasmas? *Journal of Physics D: applied physics* 36, 3125
- Williams, R. L. (1957). Ionic mobilities in argon and helium liquids. *Canadian Journal of Physics* 35, 134–146. doi:10.1139/p57-017
- Yoshino, K., Sowada, U., and Schmidt, W. F. (1976). Effect of molecular solutes on the electron drift velocity in liquid Ar, Kr, and Xe. *Physical Review A* 14, 438–444. doi:10.1103/PhysRevA.14.438

## 1 LIQUID ARGON AND XENON DATA

The following tables present details of the experimental measurements for electrons in LAr and LXe, compiled in the data repository described in Section 2.

$T$ [K]	$N$ [m <sup>-3</sup> ]	$P$ [kPa]	Ref.	$T$ [K]	$N$ [m <sup>-3</sup> ]	$P$ [kPa]	Ref.
$\mu N (E/N)$							
87.0	2.0e28	-	(Shinsaka et al., 1988)	85.0	-	608.0	(Schnyders et al., 1966)
87.0	2.1e28	-	(Huang and Freeman, 1981)	85.0	-	-	(Gushchin et al., 1982)
94.0	2.0e28	-	(Huang and Freeman, 1981)	85.0	-	-	(Halpern et al., 1967)
120.0	1.8e28	-	(Huang and Freeman, 1981)	85.0	-	-	(Miller et al., 1968)
125.8	1.7e28	-	(Eibl et al., 1990)	86.8	-	-	(Kalinin et al., 1996)
134.4	1.5e28	-	(Eibl et al., 1990)	87.0	-	-	(Buckley et al., 1989)
137.0	1.5e28	-	(Huang and Freeman, 1981)	87.0	-	-	(Pruett and Broida, 1967)
138.6	1.5e28	-	(Eibl et al., 1990)	87.0	-	-	(Walkowiak, 2000)
141.7	1.4e28	-	(Eibl et al., 1990)	87.0	-	-	(Yoshino et al., 1976)
144.2	1.3e28	-	(Eibl et al., 1990)	87.0	-	-	(Abratenko et al., 2021a)
145.0	1.3e28	-	(Huang and Freeman, 1981)	87.7	-	-	(Abi et al., 2020)
145.2	1.3e28	-	(Eibl et al., 1990)	89.8	-	-	(Walkowiak, 2000)
146.0	1.3e28	-	(Lamp and Buschhorn, 1994)	90.0	-	-	(Williams, 1957)
146.8	1.2e28	-	(Eibl et al., 1990)	90.1	-	709.3	(Schnyders et al., 1966)
147.0	1.2e28	-	(Huang and Freeman, 1981)	93.9	-	-	(Walkowiak, 2000)
147.6	1.2e28	-	(Eibl et al., 1990)	100.0	-	-	(Gushchin et al., 1982)
148.0	1.2e28	-	(Eibl et al., 1990)	120.0	-	-	(Gushchin et al., 1982)
149.0	1.1e28	-	(Huang and Freeman, 1981)	130.0	-	-	(Gushchin et al., 1982)
148.4	1.1e28	-	(Lamp and Buschhorn, 1994)	145.0	-	4590.0	(Schnyders et al., 1966)
148.4	1.2e28	-	(Eibl et al., 1990)	-	-	-	(Malkin and Schultz, 1951)
149.2	1.1e28	-	(Eibl et al., 1990)	$\mu (P)$			
150.0	1.0e28	-	(Huang and Freeman, 1981)	100.3	-	-	(Schnyders et al., 1966)
150.1	1.0e28	-	(Eibl et al., 1990)	90.1	-	-	(Schnyders et al., 1966)
150.5	9.8e27	-	(Eibl et al., 1990)	105.3	-	-	(Schnyders et al., 1966)
150.8	9.2e27	-	(Eibl et al., 1990)	111.5	-	-	(Schnyders et al., 1966)
151.0	8.1e27	-	(Huang and Freeman, 1981)	145.0	-	-	(Schnyders et al., 1966)
151.0	8.1e27	-	(Eibl et al., 1990)	$D_T/\mu (E/N)$			
151.0	8.6e27	-	(Eibl et al., 1990)	89.0	-	-	(Li et al., 2016)
89.0	-	-	(Li et al., 2016)	-	2.1e28	-	(Shibamura et al., 1979)
$D_L (E)$							
87.0	-	-	(Abratenko et al., 2021b)	-	-	-	(Doke, 1982)

Table 1. List of all LAr data included in the database. Missing data is indicated by a hyphen.

$T$ [K]	$N$ [m <sup>-3</sup> ]	$P$ [kPa]	Ref.	$T$ [K]	$N$ [m <sup>-3</sup> ]	$P$ [kPa]	Ref.
162.0	-	$\mu(E)$	(Njoya et al., 2020)	163.0	1.4e28	$\mu N(E/N)$	(Huang and Freeman, 1978)
163.0	-	-	(Miller et al., 1968)	177.0	1.3e28	-	(Thieme, 2022)
165.0	-	-	(Gushchin et al., 1982)	184.0	1.3e28	200.0	(Baudis et al., 2018)
165.0	-	-	(Yoshino et al., 1976)	216.0	1.2e28	-	(Huang and Freeman, 1978)
167.0	-	-	(Albert et al., 2017)	278.0	8.6e27	-	(Huang and Freeman, 1978)
173.3	-	163.7	(Baur et al., 2023)	288.0	6.8e27	-	(Huang and Freeman, 1978)
173.3	-	163.7	(Baur et al., 2023)				
173.4	-	168.0	(Jörg et al., 2022)			$D_L(E)$	
173.4	-	168.0	(Jörg et al., 2022)	162.0	-	-	(Njoya et al., 2020)
177.0	-	-	(Aprile et al., 2019)	177.6	-	205.0	(Baudis et al., 2023)
177.6	-	205.0	(Baudis et al., 2023)	183.2	-	-	(Hogenbirk et al., 2018)
182.0	-	-	(Aprile et al., 2012)				
183.2	-	-	(Hogenbirk et al., 2018)			$D_T(E)$	
200.0	-	-	(Gushchin et al., 1982)	167.0	-	-	(Albert et al., 2017)
230.0	-	-	(Gushchin et al., 1982)				
-	-	-	(Swan, 1962)			$D_T(E/N)$	
				-	1.4e28	-	(Doke, 1982)

Table 2. List of all LXe data included in the database. Missing parameters are indicated by a hyphen.